AGU PUBLICATIONS

Paleoceanography

RESEARCH ARTICLE
10.1002/2013PA002567

Key Points:
- Deepwater circulation weakened and reversed during ETM2 in the Atlantic
- Post-ETM2 intensification of deep-sea currents, affecting CCD and biota
- Persistent weakened hydrological cycle affects post-ETM2 clay accumulation

Supporting Information:
- Readme
- Figure S1
- Table S1
- Table S2

Correspondence to:
S. D'haenens,
simon.dhaenens@ees.kuleuven.be

Citation:
D'haenens, S., A. Bornemann, P. Claeys, U. Röhl, E. Steurbaut, and R. P. Speijer (2014), A transient deep-sea circulation switch during Eocene Thermal Maximum 2, *Paleoceanography*, *29*, doi:10.1002/2013PA002567.

Received 25 SEP 2013
Accepted 16 APR 2014
Accepted article online 22 APR 2014

A transient deep-sea circulation switch during Eocene Thermal Maximum 2

Simon D'haenens[1], André Bornemann[2], Philippe Claeys[3], Ursula Röhl[4], Etienne Steurbaut[5], and Robert P. Speijer[1]

[1]Department of Earth and Environmental Sciences, KU Leuven, Leuven, Belgium, [2]Institut für Geophysik und Geologie, Universität Leipzig, Leipzig, Germany, [3]Earth System Sciences, Vrije Universiteit Brussel, Brussel, Belgium, [4]MARUM–Center for Marine Environmental Sciences, Bremen University, Bremen, Germany, [5]Department of Paleontology, Royal Belgian Institute of Natural Sciences, Brussels, Belgium

Abstract Ever since its discovery, Eocene Thermal Maximum 2 (ETM2; ~53.7 Ma) has been considered as one of the "little brothers" of the Paleocene-Eocene Thermal Maximum (PETM; ~56 Ma) as it displays similar characteristics including abrupt warming, ocean acidification, and biotic shifts. One of the remaining key questions is what effect these lesser climate perturbations had on ocean circulation and ventilation and, ultimately, biotic disruptions. Here we characterize ETM2 sections of the NE Atlantic (Deep Sea Drilling Project Sites 401 and 550) using multispecies benthic foraminiferal stable isotopes, grain size analysis, XRF core scanning, and carbonate content. The magnitude of the carbon isotope excursion (0.85–1.10‰) and bottom water warming (2–2.5°C) during ETM2 seems slightly smaller than in South Atlantic records. The comparison of the lateral $\delta^{13}C$ gradient between the North and South Atlantic reveals that a transient circulation switch took place during ETM2, a similar pattern as observed for the PETM. New grain size and published faunal data support this hypothesis by indicating a reduction in deepwater current velocity. Following ETM2, we record a distinct intensification of bottom water currents influencing Atlantic carbonate accumulation and biotic communities, while a dramatic and persistent clay reduction hints at a weakening of the regional hydrological cycle. Our findings highlight the similarities and differences between the PETM and ETM2. Moreover, the heterogeneity of hyperthermal expression emphasizes the need to specifically characterize each hyperthermal event and its background conditions to minimalize artifacts in global climate and carbonate burial models for the early Paleogene.

1. Introduction

The discovery of numerous carbon isotope excursions (CIEs) in the early Paleogene [*Cramer et al*., 2003; *Nicolo et al*., 2007; *Galeotti et al*., 2010; *Zachos et al*., 2010] can be considered as the prologue to the recovery of the Elmo clay layer at Walvis Ridge and the subsequent characterization of the Eocene Thermal Maximum 2 (ETM2; ~53.7 Ma) as a global hyperthermal event [*Lourens et al*., 2005]. Similarly, but with a smaller amplitude and shorter duration compared to the Paleocene-Eocene Thermal Maximum (PETM; ~56 Ma) [*McInerney and Wing*, 2011; *Speijer et al*., 2012], the ETM2 is also characterized by substantial environmental changes such as a rapid rise in surface and deep-sea temperature, shoaling of the calcite compensation depth, surface ocean acidification, precipitation and productivity changes, and substantial biotic disruptions [*Sluijs et al*., 2009; *Stap et al*., 2009, 2010; *Abels et al*., 2012; *Dedert et al*., 2012; *Stassen et al*., 2012].

Although many possible causes for the PETM and its environmental changes have been put forward, the actual driving forces remain enigmatic [*McInerney and Wing*, 2011]. However, the somewhat controversial mechanism of an abrupt change in deep-ocean circulation [*Bice and Marotzke*, 2002; *Pak and Miller*, 1992; *Thomas et al*., 2003; *Nunes and Norris*, 2006; *Zeebe and Zachos*, 2007; *Bornemann et al*., 2014] may explain the reduction of ventilation and lowered oxygen levels found globally, promoting the severe extinction of deep-sea benthic foraminifera that took place at the PETM [*Thomas*, 2007; *Winguth et al*., 2012]. No such benthic extinction has been observed for the ETM2, but several early Eocene short- and long-term benthic foraminiferal biofacies shifts associated with CIEs have been documented in the North Atlantic [*D'haenens et al*., 2012b].

The goal of this study is to characterize ETM2 in two key North Atlantic Deep Sea Drilling Project (DSDP) sites (Site 401 and Site 550) in order to test the hypothesis of a circulation switch during ETM2—as documented

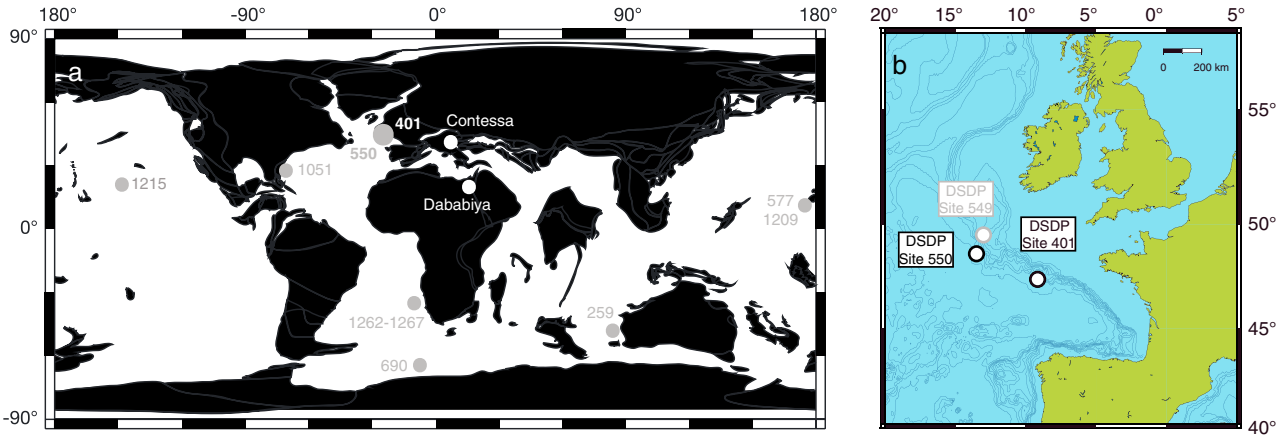

Figure 1. (a) Global paleogeographic reconstruction (~53 Ma; http://www.odsn.de/odsn/services/paleomap/paleomap.html) showing all sites mentioned in text. (b) Present-day bathymetric map of the Bay of Biscay with locations of DSDP Sites 401, 549, and 550.

for the PETM at Site 401 [*Nunes and Norris*, 2006; *Bornemann et al*., 2014]—using multispecies benthic foraminiferal isotope data in combination with grain size analyses and carbonate accumulation records.

By documenting the oceanographic boundary conditions during the earliest Eocene (including ETM2) along a bathymetric profile in the NE Atlantic, we are able to provide valuable information on the notorious geographical blind spot in Eocene climate models [*Huber et al*., 2003; *Lunt et al*., 2012]. In fact, understanding the drivers and threshold mechanisms of the ETM2 with respect to the PETM and ETM3 [*Zachos et al*., 2010; *Lunt et al*., 2011; *DeConto et al*., 2012] is vital for understanding the heterogeneity of early Eocene, especially in view of the connection of the North Atlantic Ocean to the Tethys, South Atlantic, and to the more northern waters of the Arctic [e.g., *Roberts et al*., 2009; *Cope and Winguth*, 2011].

2. Material and Methods

2.1. Sites and Material

We analyzed samples from two DSDP sites in the NE Atlantic Ocean. Site 401 (47°25.65′N, 08°48.62′W; ~42.3°N paleolatitude [*McInerney and Wing*, 2011]) is situated in the Bay of Biscay and represents a bathyal site on Meriadzek Terrace (2495 m present water depth; ~1800–2000 m paleodepth [*D'haenens et al*., 2012b]). Abyssal Site 550 on Goban Spur (48°30.91′N, 13°26.37′W; ~43.4°N paleolatitude; [*McInerney and Wing*, 2011]) represents one of the deepest (4432 m present water depth; ~3900 m paleodepth [*de Graciansky et al*., 1985]) lower Eocene carbonate-bearing locations (Figure 1). For Site 401, the studied sedimentary succession consists of lower Eocene pale grayish-brown, calcareous nannofossil marlstones covering core 13 and the lower part of core 12. Forty-nine samples were taken from an 11 m thick interval (185.00–196.00 m below seafloor (bsf)). The studied succession of Site 550 consists of the lower Eocene brownish and grayish marly nannofossil chalks of cores 29 and 30. Sixty-three samples were taken from an ~17.5 m thick interval (356.00–373.50 m bsf).

2.2. Integrated Age Model and Regional/Global Chemostratigraphic Correlation

The studied intervals of both sites span parts of calcareous nannofossil biozones NP10 to NP12 [*Cramer et al*., 2003; *Raffi et al*., 2005; *D'haenens et al*., 2012b; *Bornemann et al*., 2014]. *D'haenens et al*. [2012b] described several marly levels in the recovered part of NP11 of Site 401, of which two (β and δ; Figure 2) were suggested to reflect hyperthermal events based on a $\delta^{13}C_{bulk}$ and $\delta^{18}O_{bulk}$ record and significant benthic foraminiferal assemblage changes. However, the lack of a convincing magnetostratigraphic framework [*Hailwood*, 1979] and the recovery gap between cores 12 and 13 hampered a reliable correlation with known global CIEs occurring in biozone NP11 such as H1 (ETM2), H2, I1, I2, or J as defined by *Cramer et al*. [2003].

In contrast, Site 550 represents one of the best stratigraphically studied lower Paleogene records of the North Atlantic [*Aubry et al*., 1996; *Ali and Hailwood*, 1998; *Raffi et al*., 2005; *Westerhold et al*., 2009] (Figure 3) and,

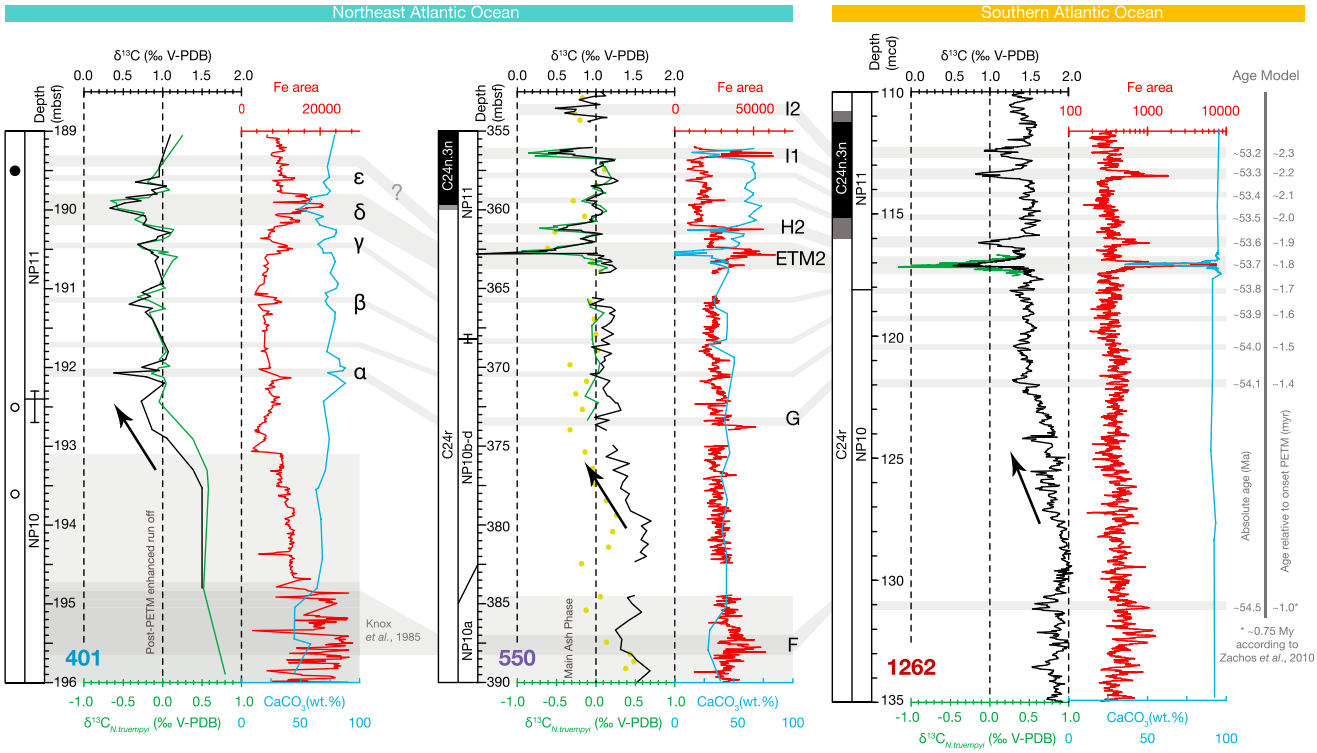

Figure 2. Long-term (NP10–NP12) stratigraphic correlation between sites of the North Atlantic (DSDP Sites 401 and 550) and the South Atlantic (IODP Site 1262). Gray bands represent short-term eccentricity cycles (~100 kyr) and visualize the correlation. Nomenclature of levels α, β, γ, δ, and ε of Site 401 from *D'haenens et al.* [2012b]; level δ corresponds to ETM2. Figure based on biomagnetostratigraphy [*Hailwood et al.*, 1979; *Ali and Hailwood*, 1998; *Raffi et al.*, 2005; *Bowles*, 2006; *Agnini et al.*, 2007; *D'haenens et al.*, 2012b], XRF core scanning (Fe) [*Westerhold et al.*, 2007, 2009], tephrostratigraphy [*Knox*, 1985], and bulk isotope chemostratigraphy [*Cramer et al.*, 2003; *Zachos et al.*, 2010; *D'haenens et al.*, 2012b]. Benthic isotopes (*N. truempyi*; green lines) from *Stap et al.* [2010] and this study. Additional *N. truempyi* data for Site 550 (green dots) from *Charisi and Schmitz* [1996]. Carbonate content from *Zachos et al.* [2004], *Stap et al.* [2009], and *D'haenens et al.* [2012b]. Note the globally observed drop of 0.5‰ in the bulk [*Cramer et al.*, 2003] and foraminiferal carbon isotope records in the upper part of biozone NP10 for all sites.

in turn, is correlated to the highly resolved stratigraphic record of Site 1262 [*Westerhold et al.*, 2007, 2009, 2012; *Zachos et al.*, 2010]. Based on the age model by *Cramer et al.* [2003], amended using *Stap et al.* [2009], *Westerhold et al.* [2009, 2012], and *Zachos et al.* [2012], we constructed an integrated age model for Site 550. Incorporating the new $\delta^{13}C$ (see section 2.3) and XRF core-scanning records (see section 2.6) of Site 401 into its biomagnetostratigraphic framework allowed for a regional correlation with Site 550 (Figure 2). We conclude that marly level δ of Site 401 is indeed ETM2, while levels α, β, γ, and ε are part of the short-term eccentricity-driven background variability (Figure 2).

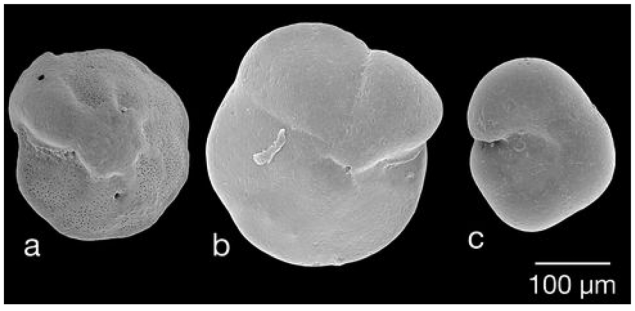

Figure 3. Scanning electron microscope (SEM) micrographs of (a) *Nuttallides truempyi* (550, 30R-1, 125–128; 369.745 m bsf), (b) *Oridorsalis umbonatus* (550, 29R-5, 125–127; 363.265 m bsf), and (c) *Quadrimorphina profunda* (550, 29R-6, 35–37,5; 363.69 m bsf).

2.3. Stable Isotopes ($\delta^{13}C$ and $\delta^{18}O$)

We performed 111 $\delta^{13}C$ and $\delta^{18}O$ measurements of benthic foraminifera for 49 samples of Site 401, including duplicates. One hundred forty measurements on benthics were carried out on 60 samples of Site 550 (see supporting information). For each measurement, we selected ~10 well-preserved specimens of *Nuttallides truempyi* (epibenthic) and *Oridorsalis umbonatus* (shallow endobenthic) from the 125–180 µm size fraction, and—if necessary—additional

specimens were picked from the 180–250 μm size fraction to reach ~50 μg. Duplicate analyses revealed no substantial ontogenetic effects on isotope values between specimens of different size. In the ETM2 interval of Site 550, we generated a splice using *Quadrimophina profunda* (endobenthic) because of the brief absence of *N. truempyi* and *O. umbonatus*. In addition, 83 analyses were carried out on bulk sediment of Site 550 to improve the chemostratigraphic correlation between sites.

Prior to analysis, all foraminifers were ultrasonically cleaned. For benthic foraminifer isotope measurements from Site 401, a ThermoFinnigan 252 mass spectrometer equipped with a Kiel III online carbonate preparation line at the Universität Erlangen, Germany, was used. Bulk sediment and benthic foraminiferal isotope measurements of Site 550 were carried out at the Vrije Universiteit Brussel (VUB), Belgium, using a ThermoFinnigan Delta^{plus} XL mass spectrometer also equipped with an automated Kiel III preparation line. Duplicate analyses on *N. truempyi* from Site 401 were run in both aforementioned labs to ensure that the results are in accordance. All values are reported in per mil relative to Vienna Peedee belemnite (VPDB) by assigning a δ^{13}C value of +1.95‰ and a δ^{18}O value of −2.20‰ to National Bureau of Standards (NBS)19. The analytical precision (1σ) based on replicate analyses of standards (NBS19 and International Atomic Energy Agency-CO1) is better than 0.040 for δ^{13}C and 0.060 for δ^{18}O (Universität Erlangen) and 0.025 for δ^{13}C and 0.035 for δ^{18}O (VUB).

In order to estimate absolute bottom water temperatures, we used the temperature equation of *Shackleton et al.* [1974] assuming an "ice-free world" where a mean value of −1.24‰ (VPDB) was estimated for deep-sea $\delta^{18}O_{sw}$, based on a mean value of −0.97‰ (SMOW) for the early Eocene [*Zachos et al.*, 1994] and corrected according to *Hut* [1987]. The $\delta^{18}O_{Ntr}$ record was corrected to *Oridorsalis umbonatus*, as the latter species secretes carbonate with δ^{18}O values close to equilibrium with seawater [*Shackleton et al.*, 1984; *Katz et al.*, 2003]. Applying the disequilibrium δ^{18}O fractionation correction of +0.35% [*Shackleton et al.*, 1984] reveals no significant difference between the two species ($\Delta\delta^{18}O_{Ntr\text{-}Oum} = 0.1435$‰ $R^2 = 0.52$, $n = 46$, $\sigma = 0.26$, and $p = 0.17$) for Site 401 and ($\Delta\delta^{18}O_{Ntr\text{-}Oum} = 0.094$‰, $R^2 = 0.56$, $n = 58$, $\sigma = 0.18$, and $p = 0.65$) for Site 550, which is well within the error range assuming both species precipitate their tests in equilibrium with seawater. Omission of the sample at 362.680 m bsf at Site 550 (likely recrystallization of *N. truempyi*) improves the $\Delta\delta^{18}O_{Ntr\text{-}Oum}$ value to 0.057‰ ($R^2 = 0.69$, $n = 57$, $\sigma = 0.18$, and $p = 0.86$). Using least squares linear regression on our data set ($\delta^{18}O_{Oum} = 0.7594 \cdot \delta^{18}O_{Qpr} + 0.0211$), we corrected *Q. profunda* to *O. umbonatus* ($R^2 = 0.51$, $n = 16$, $\sigma = 0.15$, and $p = 3.70 \cdot 10^{-4}$).

2.4. Calculation of Linear Sedimentation Rates and Mass Accumulation Rates of DSDP Site 550

Linear sedimentation rates (LSRs) were calculated using our integrated age model. Following the method of *van Andel et al.* [1975] and using wet-density (D_W) and porosity (P) data from Site 550 [*Montadert and Poag*, 1985], we calculated dry bulk densities (D_D) assuming that the total pore space is filled with seawater (density 1.025 g cm^{-3}). The following equations were used to calculate dry bulk densities and mass accumulation rates (MARs):

$$D_D = D_W - 1.025 \cdot P \quad \left(\text{g cm}^{-3}\right)$$

$$\text{MAR}_{carb} = D_D \cdot \text{LSR} \cdot \%\text{CaCO}_3 / 100$$

$$\text{MAR}_{noncarb} = D_D \cdot \text{LSR} \cdot (100 - \%\text{CaCO}_3)/100$$

$$\text{MAR}_{total} = \text{MAR}_{carb} + \text{MAR}_{noncarb} \quad \left(\text{g cm}^{-2}\text{kyr}^{-1}\right)$$

2.5. Grain Size Analysis

Twenty-three oven-dried bulk sediment samples of Site 550 were treated with 3% hydrogen peroxide and 10% acetic acid to remove both organic and calcareous components. In a second step, they were sieved through a 63 μm mesh to separate the sand fraction. The clay fraction (<2 μm) was then removed in settling tubes following the standard Atterberg method. The grain size distribution within the silt fraction (2–63 μm) was measured in 31 classes using a calibrated Laser Particle Sizer "Analysette 22" (Fritsch GmbH) at the University of Leipzig. Each sample was analyzed 3 to 4 times, and the median of the grain size distributions as well as the percentages of the 10 to 63 μm size fraction, usually referred to as sortable silt, were calculated for each sample. According to previous studies and lab internal calibration, the standard deviation between the four measurements of this device is ~0.05–0.3 μm, with a mean of 0.14 μm.

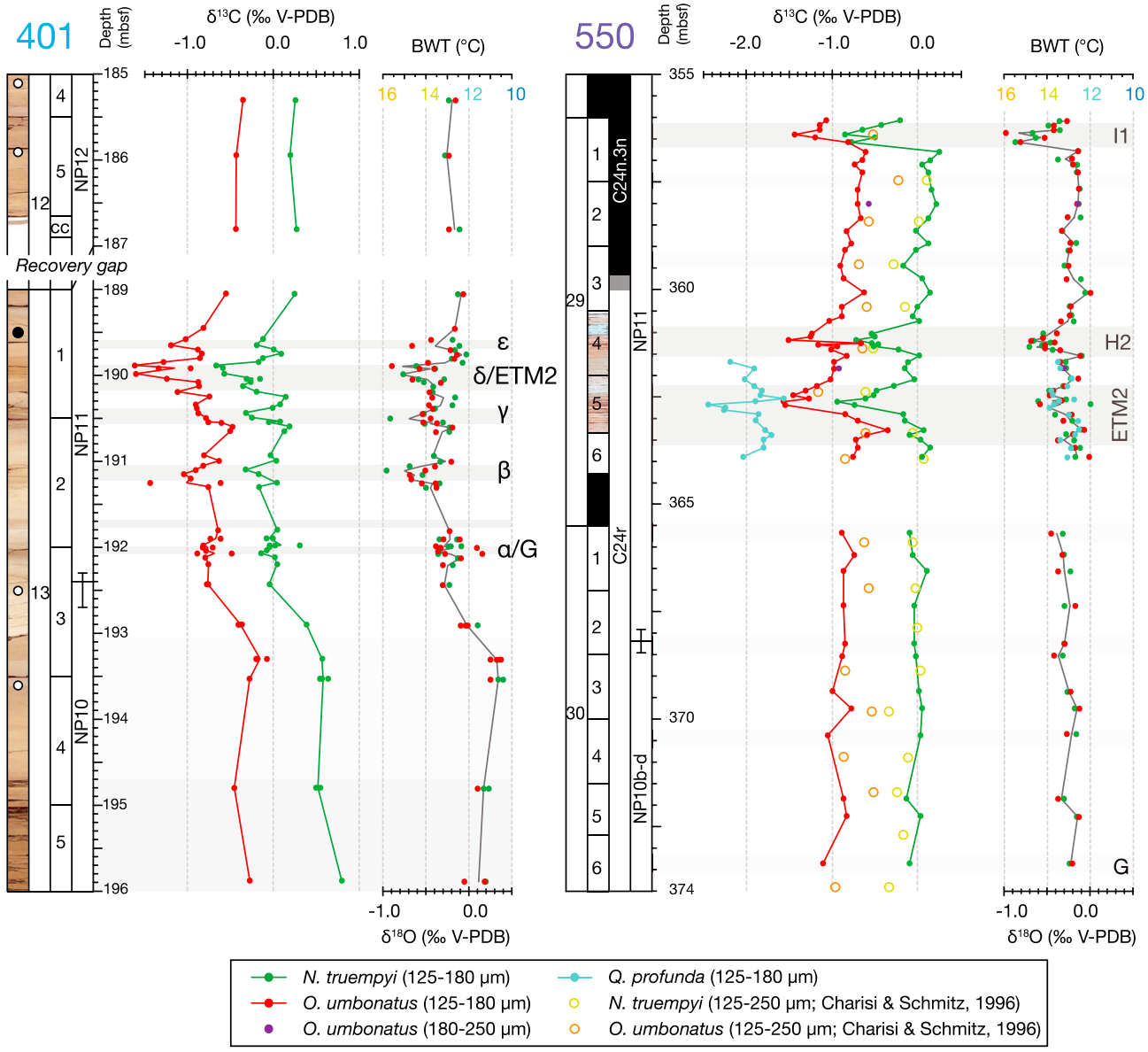

Figure 4. Stable isotope records of *Nuttallides truempyi*, *Oridorsalis umbonatus*, and *Quadrimorphina profunda* of Sites 401 and 550 plotted versus depth and biomagnetostratigraphic framework. Lines represent average values for samples with duplicate analyses. Bottom water temperatures (BWTs) are calculated with *N. truempyi* and *Q. profunda* corrected to *O. umbonatus* (see text). The α-ε nomenclature of the marly levels of Site 401 are taken from *D'haenens et al.* [2012b]. Level δ in Site 401 corresponds to ETM2 (see Figure 2).

2.6. Sediment Geochemistry

A nondestructive superslit X-ray fluorescence (XRF) core scanner equipped with an Oxford Neptune X-ray tube and a Canberra X-pips detector at MARUM–Center for Marine Environmental Sciences, Bremen University, supported by the DFG-Leibniz Center for Surface Process and Climate Studies at Potsdam University, was used to scan core 13 of Site 401. Among others, Ca, Ti, Fe, Zr, and Ba intensities were measured every centimeter downcore over a 0.5 cm^2 area. For the lighter elements Ca, Ti, and Fe, we used a generator setting of 10 kV, an X-ray current of 0.2 mA, and a sampling time of 10 s. For the heavier elements Zr and Ba, we used a generator setting of 50 kV, an X-ray current of 1.0 mA, and a sampling time of 20 s. The XRF elemental data for Site 401 exhibit variability that can be directly attributed to lithology, and highs in Fe and lows in Ca correspond to the observed isotope pattern (Figure 2). In accordance with the available chemostratigraphic, tephrostratigraphic, magnetostratigraphic, and biostratigraphic information, the XRF

core-scanning data were primarily applied to correlate Site 401 with XRF core-scanning data from Site 550 and Ocean Drilling Program (ODP) Site 1262 (Figure 2). Just like for Site 401 [*D'haenens et al*., 2012b], samples of Site 550 were analyzed for their $CaCO_3$ content using the carbonate bomb technique [*Müller and Gastner*, 1971]. The precision for replicate analyses is about 2 wt %.

3. Results

3.1. Stable Isotope Record (δ^{13}C and δ^{18}O)

In both studied sections, benthic foraminifera show similar preservation states and are generally well preserved (Figure 3). Analyzed specimens are transparent when dry and completely translucent when wet. Scanning electron microscope (SEM) imaging showed no or little etching and unfilled pore canals, if present. At both sites *N. truempyi* and *O. umbonatus* show uniform δ^{13}C and δ^{18}O values (Figures 2 and 4), confirming that the depositional loci were all bathed by seawater with similar properties (bottom water temperatures (BWTs), $\delta^{13}C_{DIC}$) and that a homogeneous intermediate/deep-sea water mass in the North Atlantic was present during the earliest Eocene [*Thomas et al*., 2003; *Cramer et al*., 2009].

3.1.1. Benthic δ^{13}C Signals

The uniformity of the benthic δ^{13}C signals at these North Atlantic intermediate to abyssal water depths is reflected in the interspecies offsets. We observe a systematic $\Delta\delta^{13}C_{Ntr\text{-}Oum}$ offset of 0.78‰ ($R^2 = 0.72$, $n = 46$, $\sigma = 0.49$, and $p = 2.39 \cdot 10^{-32}$) for Site 401 and 0.82‰ ($R^2 = 0.61$, $n = 58$, $\sigma = 0.16$, and $p = 3.07 \cdot 10^{-37}$) for Site 550, in contrast to the 0.46‰ offset value generated by *Katz et al*. [2003]. Other studies have also shown widely differing interspecies offsets [*Shackleton et al*., 1984; *Shackleton and Hall*, 1997; *Coxall et al*., 2005; *Dutton et al*., 2005]. Consequently, we attribute this difference to an ecological signal owing to the supposed opportunistic lifestyle of *O. umbonatus* [*Jorissen and Wittling*, 1999], a different local food source or the degree of decomposition of organic matter. Despite potential uncertainties in their (paleo)ecology, the different benthic species record the same paleoceanographic trends and parallel the bulk isotope record (Figures 2 and 4). *Stap et al*. [2010] also reported local fairly uniform values at Walvis Ridge, although a clear interbasinal δ^{13}C gradient of 0.50‰ between the North and South Atlantic Ocean exists in the earliest Eocene (see section 4.3.2).

Hyperthermal events ETM2, H2, and I1 are all characterized by pronounced negative δ^{13}C excursions (Figure 4 and Table S1 in the supporting information). In general, the CIEs are less pronounced at Site 401 than at 550 resembling the Walvis Ridge records where the shallowest site also registers slightly smaller δ^{13}C and δ^{18}O excursions [*Stap et al*., 2010].

3.1.2. Ecology of *Quadrimorphina Profunda*

Based on its morphology and large negative δ^{13}C offset relative to *N. truempyi* and *O. umbonatus* (Figure 4), we infer a deep endobenthic and opportunistic behavior to *Q. profunda*, supporting earlier suspicions [*Takeda and Kaiho*, 2007; *Thomas*, 2007]. The clear $\Delta\delta^{13}C_{Oum\text{-}Qpr}$ reduction of ~1.20‰ right above the clay layers in Site 550 may be indicative for a pH drop exclusively enriching δ^{13}C values of *Q. profunda*, although the shallow endobenthic *O. umbonatus* is thought to be susceptible to the carbonate ion effect as well [*Rathmann and Kuhnert*, 2008; *Uchikawa and Zeebe*, 2010]. The $\Delta\delta^{13}C_{Oum\text{-}Qpr}$ reduction, thus, argues more for an upward migration of *Q. profunda* tracking the availability of C_{org} in the sediment [*Schmiedl and Mackensen*, 2006], which is in line with inferred oligotrophic conditions during ETM2 at Site 401 [*D'haenens et al*., 2012b].

3.1.3. Early Eocene Bottom Water Temperatures

The observed trends in BWTs across biozones NP10–NP12 (Figure 4) are in line with other records for the early Eocene deep sea [*Dutton et al*., 2005; *Sexton et al*., 2006; *Zachos et al*., 2008; *Cramer et al*., 2009]. Most (composite) isotope records correct δ^{18}O values to *Cibicidoides*, whereas here the $\delta^{18}O_{Ntr}$ record is adjusted to *O. umbonatus*, rendering our calculated average background BWTs of ~12.5–13°C to be about 1.0–1.5°C higher compared to equatorial or Southern Ocean sites that are based on *Cibicidoides* or are not corrected to *O. umbonatus* for the earliest Eocene [*Dutton et al*., 2005; *Sexton et al*., 2006; *Stap et al*., 2010]. These higher temperatures for the North Atlantic are also reported by *Cramer et al*. [2009] and support the idea of a restricted exchange between Arctic and Atlantic waters during the latest Paleocene to early Eocene (i.e., "closed" Greenland-Norway seaway) driving warming of North Atlantic intermediate-depth waters [*Bice and Marotzke*, 2002; *Roberts et al*., 2009, 2011].

Assuming the absence of salinity or ice volume effects, the >0.50‰ drop in δ^{18}O values during ETM2, H2, and I1 (Figure 4) implies that BWTs repeatedly rose by >2.0°C to peak temperatures over 15°C, which is on par

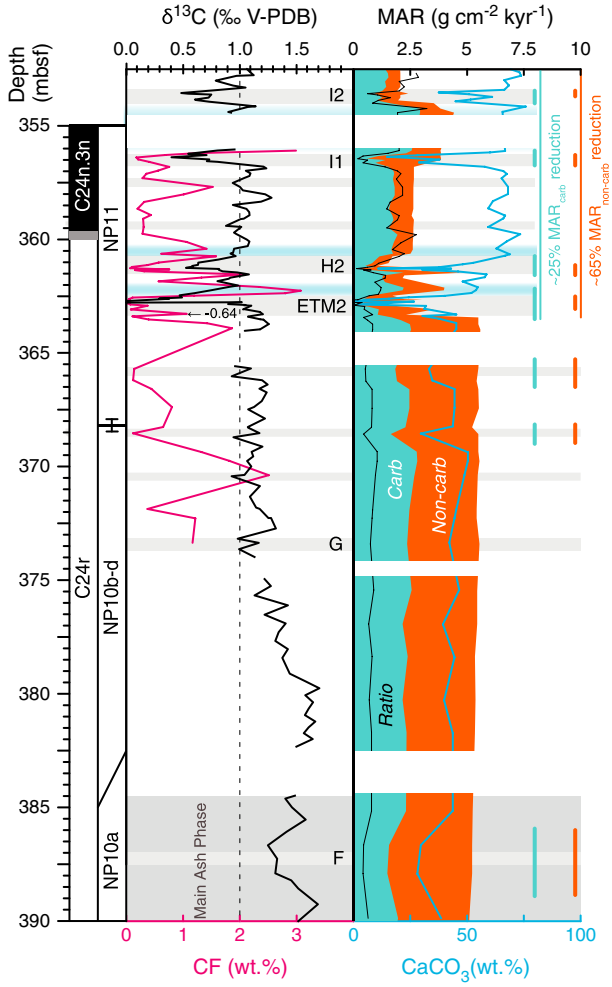

Figure 5. Mass accumulation rates (MARs) for the carbonate (teal) and non-carbonate (orange) fraction of Site 550. A dramatic drop of $MAR_{noncarb}$, and to a lesser extent MAR_{carb}, is initiated at ETM2 and lasts up to ETM3 (see supporting information). Also note the MAR_{carb} drop within each hyperthermal (ETM2, H2, I1, and I2) and during CIE F and ~ 100 and 200 kyr prior to ETM2 owing to dissolution. The thin black line represents the $MAR_{carb}/MAR_{noncarb}$ ratio. Carbonate content, coarse fraction (CF, >63 μm), and bulk $\delta^{13}C$ values for reference.

with benthic foraminiferal temperatures from the South Atlantic for ETM2 [*Stap et al.*, 2010]. Minor indications of recrystallization of foraminiferal shells are apparent in the uppermost clay layer of Site 550 (sample at 362.680 m bsf). By analogy with ETM2 values in Site 401 and I1 of Site 550, a temperature underestimation of possibly 0.5–0.75°C may be in effect. Unrelated to preservation variations, we also document a midhyperthermal cooling of ~1°C in ETM2 in both sites, similar to the more pronounced signal in the Arctic [*Sluijs et al.*, 2009]. The significance and meaning of this feature remains enigmatic, but it probably relates to local regional shifts in the structure of the water column. Nevertheless, the sudden increase by ~2–2.5°C of BWTs to near-identical temperatures in both the South and North Atlantic implies that deep waters were uniformly warmed during ETM2.

3.2. Sedimentology of Site 550

3.2.1. Carbonate Content Variations

In the abyssal Site 550—the deepest complete ETM2 sequence—we observe carbonate content variability on two time scales. The long term reveals that prior to ETM2 (starting at the PETM recovery), carbonate content fluctuates between ~30 and 50% (average of ~41%; σ: 6.37%: $n = 30$) while an immediate and prolonged carbonate increase is documented at the ETM2, as values increase by >20% to ~65–75% (Figure 5). Gradually, these carbonate values decrease, but it is not until ETM3 (~52.8 Ma) before they are restored to pre-ETM2 levels (supporting information). Independent of this long-term signal are the successive orbitally paced (~100 kyr) dissolution events, of which the most obvious ones are related to hyperthermals ETM2 and ETM3 (0% $CaCO_3$), H2, I1 and J (10–15% $CaCO_3$), and I2 (~35% $CaCO_3$) (Figure 5; supporting information). Note that a carbonate-bearing level (up to ~25%), yet virtually deprived of *Nuttallides* and *Oridorsalis*, exists between the double clay layer in the ETM2 core (see section 4.1; Figure 6).

3.2.2. LSRs and MARs

LSRs are high preceding ETM2 (average of 3.42 cm kyr^{-1}; σ: 0.05 cm kyr^{-1}; maximum values of 3.49 cm kyr^{-1}), likely representing current-driven sediment focusing [*McCave and Hall*, 2006], while during and following ETM2, these LSRs are reduced by ~50% and average 1.70 cm kyr^{-1} (σ: 0.93 cm kyr^{-1}) and 1.71 cm kyr^{-1} (σ: 0.53 cm kyr^{-1}), respectively. As expected, a similar pattern in MAR_{tot} is observed: in the interval preceding ETM2, MAR_{tot} values average 5.41 g cm^{-2} kyr^{-1} (σ: 0.13 g cm^{-2} kyr^{-1}), virtually identical to present-day Goban Spur values [*van Weering et al.*, 1998; *Antia et al.*, 1999; *McCave et al.*, 2001], whereas in the aftermath of ETM2/H2, these values are reduced to 2.77 g cm^{-2} kyr^{-1} (σ: 0.67 g cm^{-2} kyr^{-1}) (Figure 5).

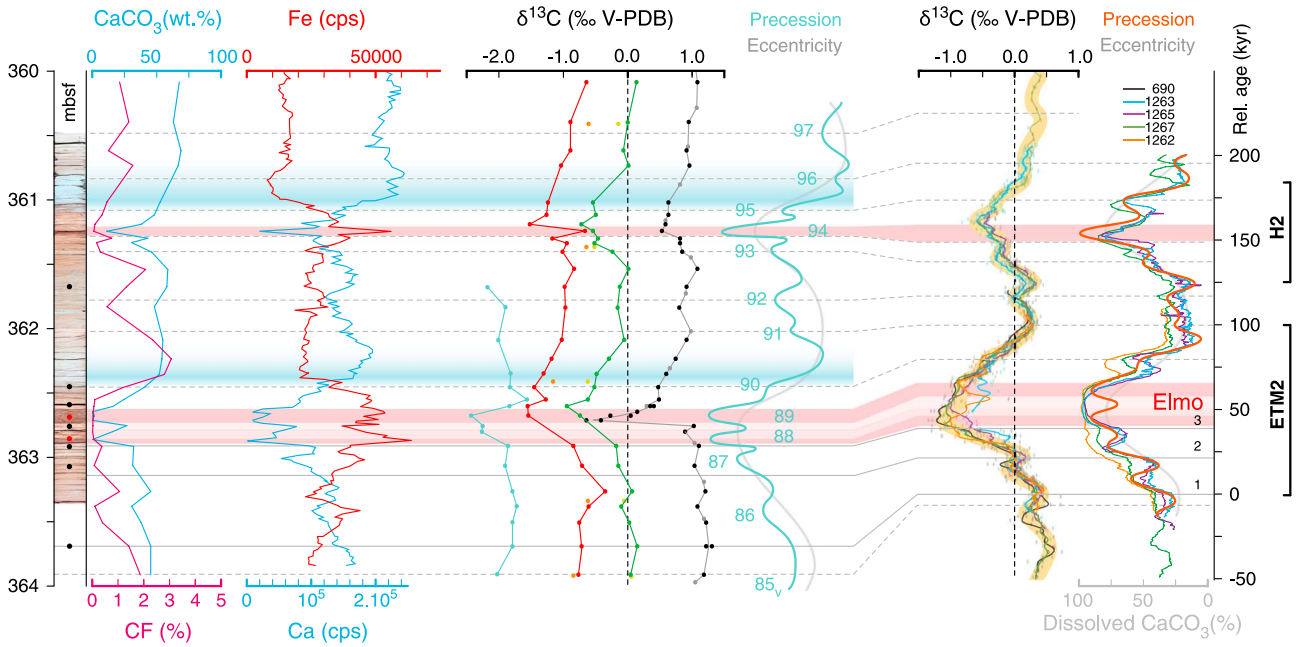

Figure 6. Sedimentological and geochemical data for the ETM2 interval of Site 550. $CaCO_3$ percentage, coarse fraction (CF, >63 μm), and XRF core-scanning data (Fe and Ca) track the lithology and reveal the double clay layer of ETM2. Values of $\delta^{13}C$ are given for *Q. profunda* (teal), *O. umbonatus* (red), *N. truempyi* (green), and bulk isotopes (black). The extracted precession and eccentricity cycles are based on XRF core-scanning data [*Westerhold et al.*, 2009]. The relative age model by *Stap et al.* [2009] based on the percentage of dissolved carbonate is used in the framework of our integrated age model to correlate this interval with the *N. truempyi* $\delta^{13}C$ values of ETM2 of Walvis Ridge and Maud Rise sites [*Stap et al.*, 2010]. Note that the single Elmo clay layer of Walvis Ridge correlates with two clay layers in Site 550, encompassing two precession cycles.

MAR_{carb} sees a permanent ~25% reduction (from 2.24 to 1.69 g cm^{-2} kyr^{-1}) at the ETM2 and remains fairly stable thereafter (apart from the discrete dissolution events accompanying ETM2, H2, I1, and I2). The relatively stable MAR_{carb} following ETM2 is in contrast with observations and modeling studies predicting an increased carbonate accumulation associated with a carbonate overshoot following ETM2 [*Dickens et al.*, 1997; *Zeebe et al.*, 2009; *Leon-Rodriguez and Dickens*, 2010; *Murphy et al.*, 2010; *Dickens*, 2011]. However, we do see a short-lived (~20 kyr) increase in coarse fraction (>63 μm) following each consecutive hyperthermal (ETM2, H2, and I1), either owing to elevated fluxes of planktic forams and/or the suppression of fine fraction (<63 μm) coccolithophoroid carbonate or the relative larger size of planktic forams due to oligotrophic conditions [*Kaiho et al.*, 2006] (Figures 5 and 6). We also note that 100 and 200 kyr prior to ETM2, minor MAR_{carb} drops occur associated with short-term eccentricity dissolution (Figure 5). Similar to MAR_{carb}, $MAR_{noncarb}$ drastically decreases by >65% (from 3.17 to 1.08 g cm^{-2} kyr^{-1}) at the onset of ETM2 (Figure 5). This state change lasts at least up to ETM3 (supporting information).

3.2.3. Grain Size Analysis

The grain size distribution of the silt size fraction has been successfully used as a current speed indicator in modern and subrecent settings [*Ledbetter and Johnson*, 1976; *Ledbetter*, 1986; *McCave et al.*, 1995]. In the interval of ETM2 of Site 550, we observe a slight decrease of the median of the silt size fraction (2–63 μm) from ~8.6 μm to ~6.3 μm, followed by long-term increase in grain size with median values >11 μm at the top of the studied interval (Figure 7). In addition, ETM2 samples are slightly better sorted than the samples below (Figure 7). The minimum values for the grain size medians during ETM2 are significantly different from the background values as indicated by a nonparametric Mann-Whitney test ($p < 0.05$). The overall trend in the median strongly covaries with the percentages of the sortable silt fraction ($R^2 = 0.99$ and $p < 0.001$), which is also used as an index of current-controlled grain size selection [*Diekmann and Kuhn*, 2002; *McCave and Hall*, 2006] (Figure 7). Site 550 is located on the abyssal plain and characterized by high sedimentation rates arguing against high amounts of turbulences, so we relate the observed change in the grain size distribution to a reduction in the average bottom water flow speed.

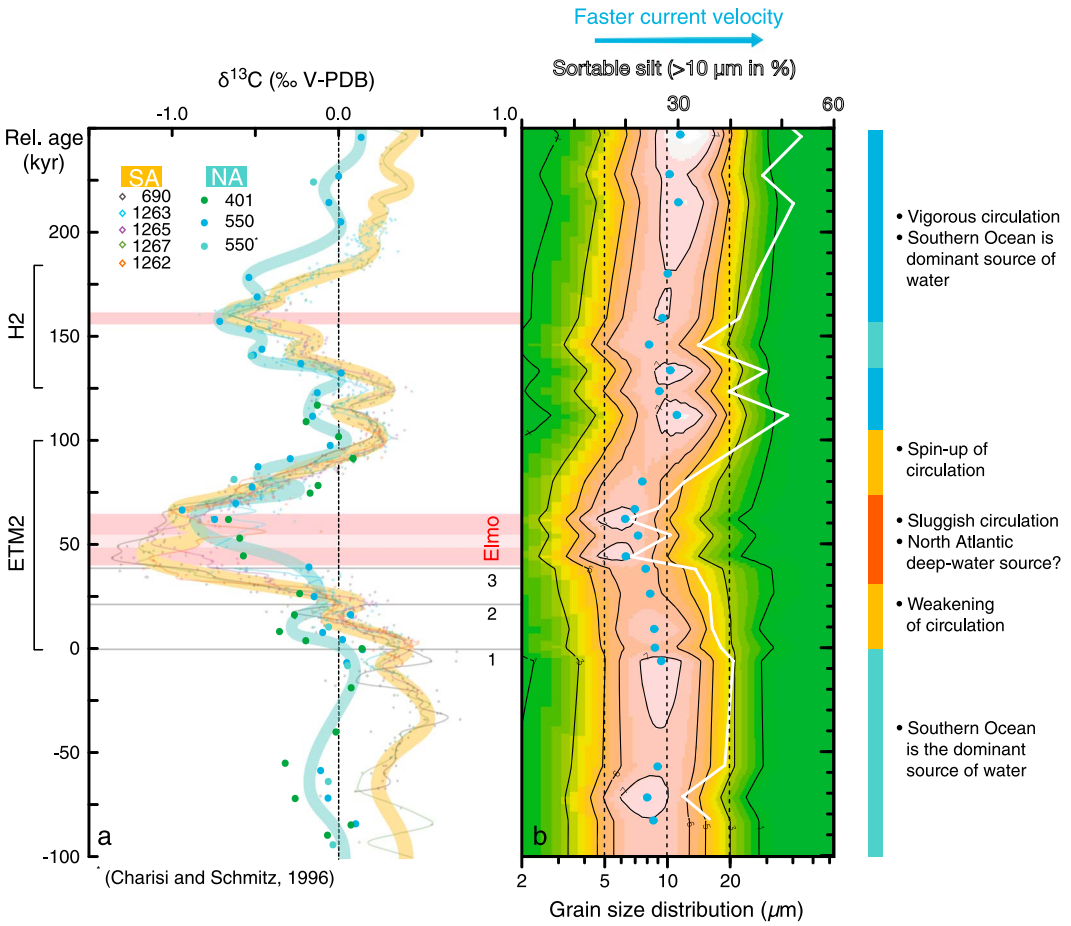

Figure 7. North and South Atlantic ETM2 $\delta^{13}C$ records on a common time scale. (a) Values of $\delta^{13}C$ of *N. truempyi* in the ETM2 interval (plotted on the common age scale of *Stap et al.* [2009, 2010]) reveal the gradual reversal of the meridional $\delta^{13}C$ gradient. The thin lines represent average $\delta^{13}C$ South Atlantic values, whereas the North Atlantic values are shown as blue and green dots. The blue and yellow envelopes surrounding the averages represent the regional signal. (b) The associated shift of >2 μm of the grain size distribution (contour plot, 2–63 μm), median values (blue dots), and the decrease of the percentage of the sortable silt fraction (10–63 μm; white line) support the isotopic reversal and illustrate the slowdown of bottom water circulation at Site 550 during ETM2. The subsequent increase in grain size distribution reflects a more vigorous circulation following ETM2.

4. Discussion

4.1. Shape and Timing of ETM2

Based on the carbonate content, isotopic and XRF core-scanning records, and in contrast to the PETM, the overall shape of ETM2 at Sites 401 and 550 is roughly symmetrical (Figures 2, 4, 6, and 7) and thus similar to what is observed worldwide in a wide range of depositional settings [*Lourens et al.*, 2005; *Nicolo et al.*, 2007; *Stap et al.*, 2009, 2010; *Galeotti et al.*, 2010; *Abels et al.*, 2012]. We observe a double peak in the XRF_{Fe} record of Sites 401 and 550 (Figures 2, 6, and S1), a feature also observed in the XRF_{Fe} records of western Atlantic Site 1051 [*Röhl et al.*, 2003] and equatorial Atlantic Site 1258 [*Westerhold et al.*, 2007, 2012]. In contrast to these sites, this doubling is clearly lithologically expressed in Site 550 where an ~11 cm thick red clay layer (362.74–362.63 m bsf) tracks a first ~3 cm thick carbonate-devoid red clay layer (362.86–362.89 m bsf) (Figure 6). Similar lithological sequences exist in the northern Tethys, where two discrete clay-rich layers make up the ETM2 as well [*Galeotti et al.*, 2010; *Coccioni et al.*, 2012]. There are no lithological or geochemical indications to suggest that synsedimentary processes have produced a duplication [e.g., *Westerhold et al.*, 2012].

Based on our integrated age model and correlation, we identify the first red clay layer as precession cycle 88 relative to the onset of the PETM and the second, thicker one as cycle 89 (Figure 6) in accordance with

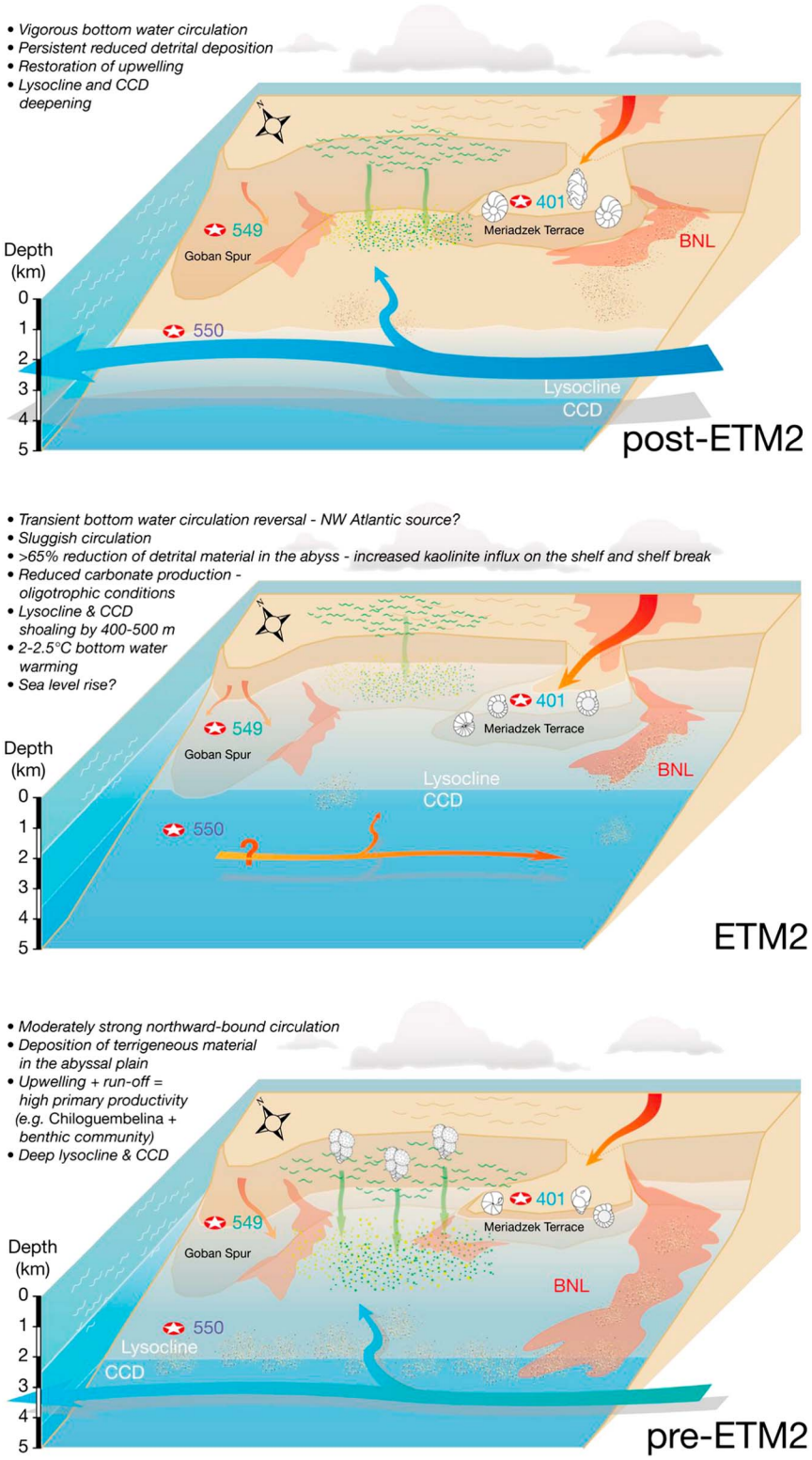

Figure 8. Synthesizing cartoon depicting the paleoceanographic changes associated with ETM2 in the Bay of Biscay, NE Atlantic Ocean. The question mark indicates the uncertainty of deep-sea current sources. BNL = bottom nepheloid layer. Note the permanent disappearance of *Chiloguembelina* (planktic foraminifer, indicator for high-nutrient environments) from the northern margin of the Bay of Biscay at the onset of ETM2. Benthic foraminiferal cartoons illustrating assemblage changes are taken from *D'haenens et al.* [2012b].

Westerhold et al. [2012]. This may imply that the single clay layer "Elmo" found in the Walvis Ridge sites (and Site 690) is indeed a result of bioturbation, mixing both clay layers [*Stap et al*., 2009]. Either way, the two distinct clay layers at Site 550, reflecting two dissolution events, would support the hypothesis of a multiple-pulsed or prolonged injection of carbon, as it would extend the total duration of dissolution and recovery compared to similar single-pulsed releases [*Zeebe*, 2013].

4.2. Evolution of the Calcite Compensation Depth During ETM2

Judging by the low carbonate values (~41%) between PETM and ETM2 of Site 550 and the large distance from the hinterland, we place this site below the lysocline but well above the carbonate compensation depth (CCD). Nearby Site 549 (paleodepth ~2500 m) displays somewhat higher, less variable carbonate contents (~46%, σ: 3.5%, and $n = 17$) in the same time interval [*Thomas and Bralower*, 2005]. The carbonate content of Site 401 is mainly driven by dilution with terrigenous material, yet the high carbonate percentages (~80%) and foraminiferal preservation prior to ETM2 suggest little influence from the lysocline [*D'haenens et al*., 2012b]. These lines of evidence suggest that prior to ETM2, the CCD was located below 3900 m, while the top of the lysocline was probably located slightly above 2500 m water depth, producing an expanded lysocline to CCD zone (Figures 5 and 8).

However, during ETM2, severe carbonate dissolution took place in the double clay layer of Site 550, resulting in carbonate-free horizons, while carbonate values of ~25% are recorded in between. Similar values (~22%) are registered in a time-equivalent ETM2 layer at Site 549 [*Masson et al*., 1985; *Thomas and Bralower*, 2005]. Site 401 experiences only minor dissolution during ETM2 [*D'haenens et al*., 2012b], if at all. Although the temporal variability of terrigenous input at Site 549 is unknown, these observations suggest that the CCD rose intermittently above 3900 m while the lysocline rose well above 2500 m, closely or possibly slightly above 2000 m (Figures 5 and 8), and we tentatively provide an estimate for lysocline and CCD shoaling during ETM2 of only 400–500 m, about a fourth as seen for the South Atlantic PETM [*Zachos et al*., 2005].

Following ETM2, all studied sites of the Bay of Biscay record a prolonged interval of homogeneous carbonate values ranging between 67 and 72%. Although this may in part be explained by the drastic reduction in $MAR_{noncarb}$ (Figure 5), it remains remarkable that across widely differing bathymetries and distances from the coastline similar carbonate values are produced. We interpret this as evidence for a deep lysocline (~3.5–4 km) in the NE Atlantic. This is consistent with the view that at the close of ETM2 the lysocline subsided below its pre-ETM2 depth, driven by enhanced global continental weathering [*Dickens et al*., 1997; *Stap et al*., 2009]. However, at the carbonate-rich sites of Walvis Ridge (>90–95% $CaCO_3$ prior to and following ETM2), major carbonate dissolution is apparent at all depths during ETM2 (~1500–3600 m paleodepth), yet complete carbonate dissolution is not observed [*Stap et al*., 2009].

4.3. Carbon Isotope Signals

4.3.1. Local Productivity Changes and Its Influence on Benthic $\delta^{13}C$

In recent deposits, it has been shown that seasonality of productivity may exert a significant force (Mackensen effect) on the $\delta^{13}C$ value of some epibenthic species such as *Cibicidoides wuellerstorfi* [*Zarriess and Mackensen*, 2011] and *Epistominella exigua* [*Corliss et al*., 2006] of up to −0.40‰. So far, there are no indications that the $\delta^{13}C$ values of either epibenthic *N. truempyi* or the shallow endobenthic *O. umbonatus* are sensitive to seasonal pulses of food. Despite their different ecologies, $\Delta\delta^{13}C_{Ntr\text{-}Oum}$ values remain stable throughout the ETM2, H2, and I1 of Sites 401 and 550 (Figure 4) and the PETM and ETM2 of the Walvis Ridge sites [*McCarren et al*., 2008; *Stap et al*., 2010], independent of contemporaneous productivity changes [*Thomas*, 1990; *Thomas and Shackleton*, 1996; *Winguth et al*., 2012]. As such, we find no indications that argue for a major influence of seasonality/productivity on the $\delta^{13}C$ signal of *N. truempyi* (and *O. umbonatus*) during the nadir of ETM2, enabling a reliable intrabasinal $\delta^{13}C_{Ntr}$ comparison.

4.3.2. Lateral $\delta^{13}C$ Gradient Changes

Lateral gradients in deepwater $\delta^{13}C$ are commonly used to determine aging of deep water and, ultimately, ocean circulation [e.g., *Curry and Oppo*, 2005; *Galaasen et al*., 2014]. This is based on the idea that the $\delta^{13}C$ signature of deep waters (i.e., deep-sea benthic foraminiferal $\delta^{13}C$) reflects the amount of organic matter remineralization sustained in the deep ocean. The longer water masses remain isolated from the surface, the

more nutrients (and ^{12}C) they acquire. As a result, "old" deep waters generally have a more negative $\delta^{13}C$ signature as they move away from their sites of formation [e.g., *Kroopnick*, 1985].

In contrast to the Late Cretaceous and the late Paleogene-Neogene, early Paleogene oceans are thought to be relatively homogeneous, because they display only small interbasinal isotopic differences of ~0.5% [*Cramer et al*., 2009; *Friedrich et al*., 2012]. Although these minor isotopic gradients are hard to interpret with regards to patterns of deepwater circulation, previous isotopic (fish teeth ε_{Nd} and foraminiferal $\delta^{13}C$) and modeling studies have shown that during the Cretaceous up to the early Paleogene (67–55 Ma), a more dominant component of southern deep water characterized the Atlantic Ocean with only a small component of northern waters [*Pak and Miller*, 1992; *Corfield and Norris*, 1996; *Bice and Marotzke*, 2002; *Thomas et al*., 2003; *Nunes and Norris*, 2006; *Via and Thomas*, 2006; *Thomas et al*., 2008; *Lunt et al*., 2010; *Hague et al*., 2012; *Robinson and Vance*, 2012]. In other words, deepwater formation primarily occurred in the Southern Hemisphere, including the South Atlantic, and flowed northward to the northern high latitudes. Our data show that NE Atlantic sites have long-term $\delta^{13}C_{Ntr}$ values of ~0.00‰ throughout the top of NP10 to NP12, while South Atlantic data sets reveal values of 0.30–0.50‰ [*Kennett and Stott*, 1990; *Stap et al*., 2010]. These $\delta^{13}C_{Ntr}$ gradients of up to −0.50‰ are well in line with published data [*Cramer et al*., 2009] and confirm that the Southern Ocean was a source area of deep water in the earliest Eocene (Figure 7).

At the onset of ETM2, Atlantic $\delta^{13}C_{Ntr}$ values start to decrease in both hemispheres but interestingly less pronouncedly in the North Atlantic (Figure 7). About 30 kyr after the onset, South Atlantic values become more negative than North Atlantic ones. In the nadir of ETM2 (40–65 kyr after the onset), $\delta^{13}C_{Ntr}$ values are ~ −0.65‰ and ~ −0.75‰ at Sites 401 and 550, respectively, while bathyal and abyssal sites in the South Atlantic reach similar or slightly more negative values (−0.75‰ to −1.10‰) (Figure 7). The southernmost location, Site 690, records the lowest average absolute values of ~ −1.25‰ [*Stap et al*., 2010].

Of course, incomplete successions or diagenetic overprints may inhibit a proper chemostratigraphic correlation and produce an artificial $\delta^{13}C$ gradient [*McCarren et al*., 2008]. Despite the slightly recrystallized *N. truempyi* specimens in the second clay layer of Site 550 (362.680 m bsf), we assume that the diagenetic overprinting signal on $\delta^{13}C$ is minimal in the ETM2 as the more dissolution-resistant species *O. umbonatus* and *Q. profunda* register similar trends. Furthermore, two intermediate $\delta^{13}C$ values for *Q. profunda* bridge the gap between the two clay layers and support the idea that the most negative $\delta^{13}C$ values have been recorded in the uppermost clay layer of Site 550 (Figure 6). Assuming the studied sites are representative for the North Atlantic basin, these values show that over the course of ~50 kyr, Atlantic intrabasin latitudinal $\delta^{13}C$ gradients changed from about −0.50‰ prior to 0.00–0.50‰ during ETM2, resulting in a short-lived reversal of meridional $\delta^{13}C$ gradients in the order of 0.50 –1.00‰ (Figure 7).

4.3.3. A Deepwater Circulation Reversal During ETM2

The interpretation of these meridional $\delta^{13}C$ gradients in function of deepwater circulation implies that during ETM2 the influence of the predominant northward bound southern deepwater current weakened and was subsequently replaced by a weak northern source, possibly originating from the Newfoundland-Labrador Sea [*Roberts et al*., 2009]. Additionally, grain size analysis of Site 550 reveals an ~2.3 μm reduction in median silt size, accompanied by a decrease of the sortable silt fraction percentage, particularly within the two red clay layers of ETM2, reflecting two short-lived phases of current speed reduction (Figure 7) [*Ledbetter*, 1986; *McCave and Hall*., 2006]. This slowdown is in agreement with the transient occurrence of an impoverished benthic foraminiferal fauna dominated by *Nuttallides umbonifera* at nearby Site 401, signifying a decrease in upwelling intensity and a short-lived sluggish circulation [*D'haenens et al*., 2012b]. We exclude eolian dust input as a significant influence to the grain size distribution curves, as maximum dust accumulation in the open ocean is typically an order of magnitude less than the $MAR_{noncarb}$ estimates for Site 550 (Figure 5) [*Rea*, 1994].

We note that the lack of regional grain size measurements along a depth transect limits our interpretation; we can only infer a reduction of flow speed at Site 550 without confirming the direction, source(s), and bathymetric range of this particular current in the water column. Furthermore, the lack of global detailed stratigraphically constrained benthic $\delta^{13}C$ records bracketing ETM2 is unfavorable to confidently resolve this [*Sexton et al*., 2006; *Hancock et al*., 2007; *Dickens and Backman*, 2013]. In fact, early Eocene deepwater flow

patterns are complex, and deepwater formation in the Atlantic Ocean may have been multimodal [*Huber et al*., 2003; *Sexton et al*., 2006; *Thomas et al*., 2008; *Roberts et al*., 2009, 2011], enabling a different circulation pattern to produce similar δ^{13}C gradients. Nevertheless, we consider the process of a transient shift in deepwater source area during ETM2 the most parsimonious solution to account for the 0.50 to 1.00‰ meridional δ^{13}C gradient discrepancy.

4.4. Long-Term Changes in the Aftermath of the ETM2

4.4.1. Spin-Up of Circulation

Following ETM2, the meridional δ^{13}C gradient is apparently restored to pre-ETM2 patterns, with slightly smaller lateral δ^{13}C gradients of ~0.30‰ (Figure 7). By analogy of pre-ETM2 conditions, this would imply that the northward advection of southern deep water is reestablished. Even more so, the decreased "age" differences between the two locations may indicate a strengthening of current velocity. Indeed, the long-term increase in grain size with median values >11 μm following ETM2 (Figure 7) indicates a prolonged increase in current velocity which is also reflected by benthic assemblages (Figure 8) [*D'haenens et al*., 2012b]. Altering bottom water hydrodynamics and sediment transport and deposition implies that some processes of eliminating bottom nepheloid layers, rerouting currents, or a more vigorous advection of intermediate and deep waters must have existed [*McCave et al*., 2001; *McCave and Hall*, 2006] (Figure 8). It is striking that large hiati in the aftermath of ETM2 occur at Site 690 [*Thomas*, 1990; *Cramer et al*., 2003; *Stap et al*., 2010], just like they do in the recovery of the PETM of Sites 550 and 690 [*Westerhold et al*., 2009; *Kelly et al*., 2012]. Possible winnowing, nondepositional, and/or erosional processes highlight the similarities with late Eocene hiatuses, preceding the onset of drift deposition in the North Atlantic and North Pacific, and indicating an intensification of deep-ocean currents [*Cramer et al*., 2009; *Katz et al*., 2011]. We assign this prolonged change of hydrodynamic regime to the influence of a strengthened (southern) deepwater current.

4.4.2. Circulation Intensification and the Effect on the CCD

Additional support for a long-term bottom water circulation intensification may come from the carbonate record. Deep-sea carbonate content is controlled not only by local production but also by changes in ocean/atmosphere chemistry as well as the direction and age of bottom water circulation which drives [CO_3^{2-}] and, thus, the saturation state [*Broecker and Peng*, 1982; *Lyle et al*., 1995; *Dickens*, 2000; *Zeebe and Zachos*, 2007; *Pälike et al*., 2012]. For the early Eocene, no changes in ocean carbonate chemistry due to temperature, hydrothermal activity, changing spreading rates, or weathering feedbacks have been inferred [*Dutton et al*., 2005; *Zachos et al*., 2008; *Stuecker and Zeebe*, 2010; *Komar et al*., 2013].

The remarkable shift to high and homogeneous carbonate values (~67–72%) following the ETM2 in the NE Atlantic (see section 4.2) is not a standalone feature. Indeed, one might speculate that the ETM2 is positioned at a sudden but long-term transition to minor increases in carbonate content in the northern Tethys [*Galeotti et al*., 2010], the South Atlantic [*Zachos et al*., 2004; *Stap et al*., 2009] (Figure 3) and equatorial Pacific [*Leon-Rodriguez and Dickens*, 2010], and at a minor drop in carbonate content in Site 259 in the SE Indian Ocean [*Hancock et al*., 2007]. We argue that dissolution of post-ETM2 biogenic calcite may have been reduced due to a more vigorous ocean circulation, producing "younger" and less corrosive water masses in the Atlantic Ocean. Incorporating additional early Paleogene (North) Atlantic CCD reconstructions into existing coupled carbon cycle models will hopefully shed light on the complex relation between hyperthermal events, carbonate preservation, and long-term circulation changes [*Pälike et al*., 2012; *Zeebe*, 2012; *Komar et al*., 2013].

4.4.3. Possible Sea Level Rise or Hydrological Changes?

The long-term reductions in MARs (Figure 5) lend some support to the idea of a significant spin-up of ocean currents, although they can also be interpreted in function of a small sea level rise or hydrological changes. On the one hand, a sea level rise (eustatic or by thermal expansion) may decrease the flux of terrigenous components to the seafloor (Figure 5)—as it has done in the recent past at Goban Spur [*van Weering et al*., 1998]. Sea level changes also promotes the relocation of carbonate burial from the deep sea to the shelf [*Ridgwell and Zeebe*, 2005; *Sluijs et al*., 2013]. However, although significant sea level rises have been inferred for the earliest Eocene [*Miller et al*., 2005, 2011; *Kominz et al*., 2008], a clear relation with the ETM2 has not been established yet [*Sluijs et al*., 2008].

On the other hand, a decrease in runoff driven by changes in the hydrological cycle would deprive the open ocean of valuable nutrients, in turn suppressing primary productivity [*Chavez et al*., 2011; *Ziegler et al*., 2013].

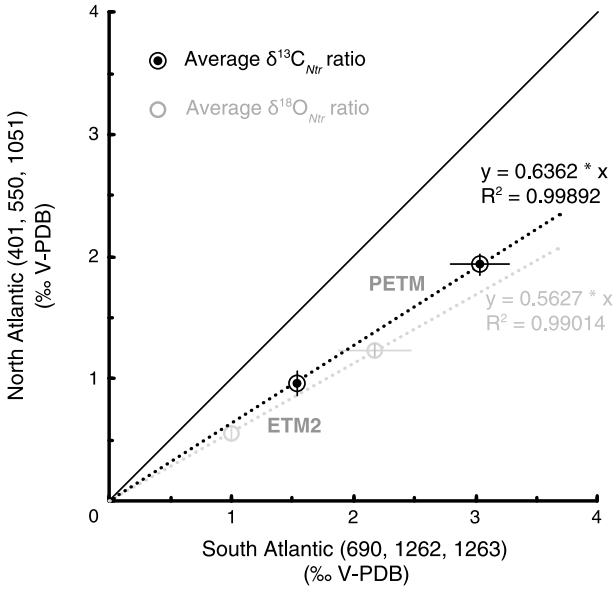

Figure 9. Comparison of the $\delta^{13}C$ and $\delta^{18}O$ magnitudes during PETM and ETM2 for the South and North Atlantic. The consistent PETM-ETM2 relation illustrates the dampened CIE and warming of both events in the North Atlantic compared to the South Atlantic. Intercepts of the linear trend lines are forced to 0. Uncertainty intervals (horizontal and vertical lines) through the data points represent 1 standard deviation (1σ).

The concurrent MAR_{carb} and $MAR_{noncarb}$ reductions at Site 550 (Figure 5) and the reduction of buliminids at Site 401 are in line with this idea [*D'haenens et al.*, 2012b]. However, uniform and Atlantic-wide ~30% reductions in LSRs immediately following ETM2 (Table S2) would suggest a latitudinally independent and homogeneous response of the hydrological cycle, conflicting with Eocene climate models [e.g., *Loptson et al.*, 2014]. A regional decrease in runoff may explain the observed MAR patterns at Site 550 more adequately. It turns out that an intensification of the hydrological cycle in the (aftermath of the) PETM led to a persistent regional increase in terrestrial runoff [*Bornemann et al.*, 2014]. Interestingly, the opportunistic planktic foraminifer *Chiloguembelina* first appeared in large numbers at the onset of the PETM at Site 401 [*Pardo et al.*, 1999; *D'haenens et al.*, 2012a], only to permanently disappear concurrent with ETM2 (Figure 8). Although no direct evidence for a long-term hydrological change associated with the ETM2 is observed in the NE Atlantic (e.g., the long-term clay mineralogical assemblages remain relatively stable in the region [*Cassat*, 1979; *Chennaux et al.*, 1985]), we suspect that, by analogy with the PETM, a regionally weakened hydrological cycle may be (partially) responsible for the observed sedimentological patterns.

4.5. Comparison With the PETM and Implications for the Origin of Hyperthermals

4.5.1. Carbon Isotope Excursions

Although the $\delta^{13}C_{Ntr}$ CIE values of the PETM and ETM2 from Site 401 are smaller than at Sites 690 and 1262/1263, the ETM2/PETM $\delta^{13}C_{Ntr}$ ratio of Site 401 (0.45) is similar to Sites 690 (0.62), 1262 (0.50), and 1263 (0.43) (Figure 9 and Table S3). The relatively small CIE values of the PETM at Site 401 [*Nunes and Norris*, 2006; *Bornemann et al.*, 2014], Site 1051 (~2.1‰; missing one precession cycle [*Röhl et al.*, 2000]), and ETM2 at Site 550 support the idea that the magnitude of both hyperthermal events is indeed smaller in the deep North Atlantic than in the deep Southern Ocean. This suggests that both hyperthermals are expressed in a similar fashion, are driven by similar processes in the Southern and Atlantic Oceans, and that a meridional, rather than just a bathymetrically heterogeneity exists. In other words, the recorded isotopic signal of North Atlantic hyperthermals appears to be dampened with respect to the South Atlantic.

4.5.2. Transient Circulation Changes

Although some authors raised concerns on stratigraphic completeness and model-data interpretations [*Thomas et al.*, 2003; *Zeebe and Zachos*, 2007; *McCarren et al.*, 2008; *Kelly et al.*, 2010], many studies have suggested that during the PETM an abrupt shift in deep-ocean circulation took place, with the locus of deepwater formation shifting to the Northern Hemisphere [*Pak and Miller*, 1992; *Bice and Marotzke*, 2002; *Tripati and Elderfield*, 2005; *Nunes and Norris*, 2006; *Lunt et al.*, 2010, 2011; *Winguth et al.*, 2010; *Bornemann et al.*, 2014]. Our data suggest that a transient reversal of the "aging gradient" in $\delta^{13}C$ is not exclusive to the PETM but also may have occurred during ETM2. Furthermore, we link the larger dynamic range in lysocline depth at the South Atlantic sites during ETM2 (see section 4.2) [*Stap et al.*, 2009] to deepwater ventilation changes, as has been done for the PETM [*Bornemann et al.*, 2014].

It is striking that although the magnitude of the CIE of the PETM is more than twice that of ETM2—suggesting a larger input of ^{13}C-depleted carbon (Figure 9)—the lateral $\delta^{13}C$ gradient variations during the respective

CIEs are more or less equal [*Nunes and Norris*, 2006], arguing that the climate system is characterized by a certain "ceiling." Furthermore, the circulation switch appears to be threshold based, as no such reversal is inferred for slightly smaller CIEs events (e.g., H2 or levels α, β, and γ at Site 401 [*D'haenens et al*., 2012b]).

4.5.3. Long-Term State Changes?

Our results argue for a certain degree of similarity between the PETM and ETM2 on shorter time scales (i.e., for the duration of the CIE itself), but we also find evidence for analogous, yet opposite long-term state changes of the hydrological cycle associated with both hyperthermals in the North Atlantic [*Bornemann et al*., 2014; this study]. We note that the regional expression of a prolonged hydrological cycle state change at ETM2 does not preclude global records from displaying an intensification of deep-sea currents, in turn influencing upwelling patterns, carbonate accumulation, and biota.

Our case is supported by diverse global records: As in Site 550, Site 1209 (Shatsky Rise, central equatorial Pacific) displays a collapse of the vertical δ^{18}O gradient between *Subbotina* (thermocline dwelling) and benthic foraminifera, initiated at the ETM2 and lasting throughout the early Eocene climatic optimum (EECO) [*Charisi and Schmitz*, 1996; *Dutton et al*., 2005]. This shift has been linked to a change in ocean circulation [*Dutton et al*., 2005]. At the same time (~53.6 to 49.3 Ma), the influence of abyssal Southern Ocean waters is reduced in the equatorial Pacific, as abyssal waters from a northern Pacific source become more apparent at Site 1215 [*Thomas et al*., 2008; *Hague et al*., 2012]. The initiation of a global decline of the vertical δ^{13}C gradient—a proxy for oceanic biological pumping efficiency—points to a long-term oceanographic change associated with ETM2 [*Hilting et al*., 2008; *Sexton et al*., 2011]. It appears that the long-term consequences of the circulation intensification at the ETM2 reverberate into the EECO and prompt the question on the mechanisms of hyperthermal formation and their influence on the evolution of the early Paleogene world.

4.5.4. Origin of Hyperthermals

By now, the idea that orbital forcing superimposed on a long-term climate trend is capable of producing multiple hyperthermals is broadly supported [*Cramer et al*., 2003; *Lourens et al*., 2005; *Zachos et al*., 2010; *Lunt et al*., 2011]. One still outstanding issue is the uncertainty surrounding the role of boundary conditions such as plate configuration, terrestrial processes, and the state of seaways (e.g., Greenland-Norway Seaway, North Sea, Bering Strait, Turgay Strait, etc.), heavily influencing the outcome of climate, circulation, and geochemical models [*Huber et al*., 2003; *Roberts et al*., 2009; *Dunkley Jones et al*., 2010; *Lunt et al*., 2010, 2011; *Zachos et al*., 2010; *Cope and Winguth*, 2011; *DeConto et al*., 2012; *Pälike et al*., 2012; *Winguth et al*., 2012; *Zeebe*, 2012]. When proposing a hypothesis on the origin of the ETM2 and its relation to the PETM and the EECO, the question must be asked whether the processes involved represent a common denominator for the formation of all early Paleogene hyperthermals or are unique to the ETM2.

For instance, one of the inferred mechanisms that may have contributed to the initiation and expression of the PETM was a change in (fresh)water exchange between different basins, possibly driven by tectonics [*Bice and Marotzke*, 2002; *Roberts et al*., 2009; *Cope and Winguth*, 2011]. Changes in surface water fluxes, altering surface water salinities and densities, would influence deepwater formation and deep overturning circulation, alter upwelling loci, and influence the hydrological cycle [*Stocker and Wright*, 1991; *Roberts et al*., 2009; *Cope and Winguth*, 2011]. We tentatively conclude that a similar mechanism may have led to the initiation of the ETM2 but that the changing boundary conditions also set the stage for subsequent hyperthermals in the metastable early Paleogene world.

5. Concluding Remarks

Multispecies benthic foraminiferal δ^{13}C and δ^{18}O and bulk sediment carbonate records in the NE Atlantic bracketing the ETM2 interval (NP10–NP12) reveal that the studied sites were ventilated by a similar water mass at all times, highlighting the uniformity of this region. Further, our records reveal the following:

1. A uniform North Atlantic bottom water (2–4 km depth) temperature of 12–13°C was present throughout the earliest Eocene and was, thus, slightly warmer than the South Atlantic. Additional warming by 2–2.5°C during ETM2, H2, and I1 in the North Atlantic brings temperatures on par with South Atlantic hyperthermal temperatures.
2. Carbonate data and accumulation patterns for Sites 401, 549, and 550 reveal that lysocline and CCD fronts shoaled by an estimated 400–500 m during ETM2 in the eastern North Atlantic and significantly deepened

afterward. Similarly, as for the PETM, North Atlantic lysocline movements across ETM2 appear to be subdued compared to the South Atlantic.

3. ETM2 CIEs amplitudes range from 0.85‰ to 1.10‰ and are smaller than known from South Atlantic records. Meridional $\delta^{13}C$ gradients, grain size data, faunal records, and carbonate accumulation patterns suggest a transient interhemispheric reversal in deep-sea circulation during the ETM2 (but not for H2), similar as documented for the PETM. This implies that despite their different CIE magnitudes, the inferred circulation switch during both hyperthermals is driven and constrained by climatic thresholds.
4. Following ETM2, we observe a prolonged restoration and an invigoration of deepwater circulation. Furthermore, contemporaneous drastic reductions in clay accumulation (>65%) at Site 550 suggest a weakening of the regional hydrological cycle. Although the mechanisms responsible for the reversal and invigoration of deepwater circulation is hitherto unknown, we suspect that changes in surface water fluxes—due to tectonics and its influence on water mass exchange between oceanic basins—influenced the position and strength of deepwater convection, upwelling loci (i.e., carbonate production and C_{org} surface export), the hydrological cycle, and biotic communities.

Acknowledgments

This research used samples and data provided by the ODP. The ODP is sponsored by NSF and participating countries under the management of Joint Oceanographic Institutions (JOI). We would like to thank A. Sluijs and two anonymous reviewers for their insightful and very constructive comments. We would also like to thank M. Joachimski (University of Erlangen), M. Nicolai (KU Leuven), and D. Vanhove (KU Leuven) for assisting with picking forams or stable isotope analyses. Discussion with M. Seidel (University of Leipzig) on the grain size data is greatly appreciated. Financial support was provided by the Research Foundation Flanders (FWO-G.0422.10) to S.D., R.P.S., P.C., and E.S., the Research Fund KU Leuven (OT/08/018) to R.P.S. and E.S., the Hercules Foundation to P.C., and by the Deutsche Forschungsgemeinschaft (DFG) to A.B. (BO 2505/4) and U.R. (RO 1113/4). This research used data acquired at the XRF Core Scanner Lab at the MARUM–Center for Marine Environmental Sciences, University of Bremen.

References

Abels, H. A., W. C. Clyde, P. D. Gingerich, F. J. Hilgen, H. C. Fricke, G. J. Bowen, and L. J. Lourens (2012), Terrestrial carbon isotope excursions and biotic change during Palaeogene hyperthermals, *Nat. Geosci.*, *5*(5), 326–329, doi:10.1038/ngeo1427.

Agnini, C., E. Fornaciari, I. Raffi, D. Rio, U. Röhl, and T. Westerhold (2007), High-resolution nannofossil biochronology of middle Paleocene to early Eocene at ODP Site 1262: Implications for calcareous nannoplankton evolution, *Mar. Micropaleontol.*, *64*, 215–248, doi:10.1016/j.marmicro.2007.05.003.

Ali, J. R., and E. A. Hailwood (1998), Magnetostratigraphic (re)calibration of the Paleocene/Eocene boundary interval in Holes 550 and 549 Goban Spur, eastern North Atlantic, *Earth Planet. Sci. Lett.*, *161*, 201–213.

Antia, A. N., B. von Bodungen, and R. Peinert (1999), Particle flux across the mid-European continental margin, *Deep Sea Res., Part I*, *46*, 1999–2024.

Aubry, M.-P., W. A. Berggren, L. D. Stott, and A. Sinha (1996), The upper Paleocene-lower Eocene stratigraphic record and the Paleocene-Eocene boundary carbon isotope excursion: Implications for geochronology, in *Correlation of the Early Paleogene in Northwest Europe*, *Geol. Soc. Spec. Publ.*. vol. 101, edited by R. W. O. B. Knox, R. M. Corfield, and R. E. Dunay, pp. 353–380.

Bice, K. L., and J. Marotzke (2002), Did changing ocean circulation destabilize methane hydrate at the Paleocene/Eocene boundary?, *Paleoceanography*, *17*(2), 1–18, doi:10.1029/2001PA000678.

Bornemann, A., R. D. Norris, J. A. Lyman, S. D'haenens, J. Groeneveld, U. Röhl, K. A. Farley, and R. P. Speijer (2014), Persistent environmental change after the Paleocene-Eocene Thermal Maximum in the eastern North Atlantic, *Earth Planet. Sci. Lett.*, *394*, 70–81, doi:10.1016/j.epsl.2014.03.17.

Bowles, J. (2006), 4 data report: Revised magnetostratigraphy and magnetic mineralogy of sediments from Walvis Ridge, Leg 208. in *Proceedings of the Ocean Drilling Program, Scientific Results*, vol. 208, edited by D. Kroon, J. C. Zachos, and C. Richter, pp. 1–24, Ocean Drilling Program, College Station, Tex., doi:10.2973/odp.proc.sr.208.206.

Broecker, W. S., and T.-H. Peng (1982), *Tracers in the Sea*, Columbia Univ., Palisades, New York.

Cassat, G. (1979), 27 X-ray mineralogy from Holes 399, 400, 400A, 401, 402 and 402A of Bay of Biscay, *Initial Rep. Deep Sea Drill. Proj.*, *48*(27), 649–663.

Charisi, S. D., and B. Schmitz (1996), Early Eocene palaeoceanography and palaeoclimatology of the eastern North Atlantic: Stable isotope results for DSDP Hole 550, in *Correlation of the Early Paleogene in Northwest Europe*, Geological Society Special Publication, vol. 101, edited by R. W. O'B. Knox, R. M. Corfield, and R. E. Dunay, pp. 457–472, Geological Society, London.

Chavez, F. P., M. Messié, and J. T. Pennington (2011), Marine primary production in relation to climate variability and change, *Annu. Rev. Mar. Sci.*, *3*(1), 227–260, doi:10.1146/annurev.marine.010908.163917.

Chennaux, G., J. Esquevin, A. Jourdan, C. Latouche, and N. Maillet (1985), X-ray mineralogy and mineral geochemistry of Cenozoic strata (Leg 80) and petrographic study of associated pebbles, *Initial Rep. Deep Sea Drill. Proj.*, *80*(48), 1019–1046.

Coccioni, R., G. Bancalà, R. Catanzarit, E. Fornaciari, F. Frontalini, L. Giusberti, L. Jovane, V. Luciani, J. Savian, and M. Sprovieri (2012), An integrated stratigraphic record of the Palaeocene-lower Eocene at Gubbio (Italy): New insights into the early Palaeogene hyperthermals and carbon isotope excursions, *Terra Nova*, *24*, 380–386, doi:10.1111/j.1365-3121.2012.01076.x.

Cope, J. T., and A. M. E. Winguth (2011), On the sensitivity of ocean circulation to arctic freshwater input during the Paleocene/Eocene Thermal Maximum, *Palaeogeogr. Palaeoclimatol. Palaeoecol.*, *306*(1–2), 82–94, doi:10.1016/j.palaeo.2011.03.032.

Corfield, R. M., and R. D. Norris (1996), Deep water circulation in the Paleocene, in *Correlation of the Early Paleogene in Northwest Europe*, Geological Society Special Publication, vol. 101, edited by R. W. O'B. Knox, R. M. Corfield, and R. E. Dunay, pp. 443–456, Geological Society, London.

Corliss, B. H., X. Sun, C. W. Brown, and W. J. Showers (2006), Influence of seasonal primary productivity on $\delta^{13}C$ of North Atlantic deep-sea benthic foraminifera, *Deep Sea Res., Part I*, *53*(4), 740–746, doi:10.1016/j.dsr.2006.01.006.

Coxall, H. K., P. A. Wilson, H. Pälike, C. H. Lear, and J. Backman (2005), Rapid stepwise onset of Antarctic glaciation and deeper calcite compensation in the Pacific Ocean, *Nature*, *433*(7021), 53–57, doi:10.1038/nature03186.

Cramer, B. S., D. V. Kent, and M.-P. Aubry (2003), Orbital climate forcing of excursions in the late Paleocene–early Eocene (chrons C24n–C25n), *Paleoceanography*, *18*(4), 1097, doi:10.1029/2003PA000909.

Cramer, B. S., J. R. Toggweiler, J. D. Wright, M. E. Katz, and K. G. Miller (2009), Ocean overturning since the Late Cretaceous: Inferences from a new benthic foraminiferal isotope compilation, *Paleoceanography*, *24*, PA4216, doi:10.1029/2008PA001683.

Curry, W. B. and D. W. Oppo (2005), Glacial water mass geometry and the distribution of $\delta^{13}C$ of ΣCO_2 in the western Atlantic Ocean, *Paleoceanography*, *20*, PA1017, doi:10.1029/2004PA001021.

de Graciansky, P. C., C. W. Poag, and S. S. Party (1985), 5 Site 550, *Initial Rep. Deep Sea Drill. Proj.*, *80*(5), 251–355.

DeConto, R. M., S. Galeotti, M. Pagani, D. Tracy, K. Schaefer, T. Zhang, D. Pollard, and D. J. Beerling (2012), Past extreme warming events linked to massive carbon release from thawing permafrost, *Nature*, *484*(7392), 87–91, doi:10.1038/nature10929.

Dedert, M., H. M. Stoll, D. Kroon, N. Shimizu, K. Kanamaru, and P. Zlveri (2012), Productivity response of calcareous nannoplankton to Eocene Thermal Maximum 2 (ETM2), *Clim Past*, *8*(3), 977–993, doi:10.5194/cp-8-977-2012.

D'haenens, S., A. Bornemann, K. Roose, P. Claeys, and R. P. Speijer (2012a), Stable isotope paleoecology ($\delta^{13}C$ and $\delta^{18}O$) of early Eocene *Zeauvigerina aegyptiaca* from the North Atlantic (DSDP Site 401), *Austrian J. of Earth Sci.*, *105*(1), 179–188.

D'haenens, S., A. Bornemann, P. Stassen, and R. P. Speijer (2012b), Multiple early Eocene benthic foraminiferal assemblage and $\delta^{13}C$ fluctuations at DSDP Site 401 (Bay of Biscay—NE Atlantic), *Mar. Micropaleontol.*, *88–89*, 15–35, doi:10.1016/j.marmicro.2012.02.006.

Dickens, G. R. (2000), Methane oxidation during the Late Palaeocene Thermal Maximum, *Bull. Soc. Géol. France*, *171*(1), 37–49.

Dickens, G. R. (2011), Down the Rabbit Hole: Toward appropriate discussion of methane release from gas hydrate systems during the Paleocene-Eocene thermal maximum and other past hyperthermal events, *Clim Past*, *7*(3), 831–846, doi:10.5194/cp-7-831-2011.

Dickens, G. R., and J. Backman (2013), Core alignment and composite depth scale for the lower Paleogene through uppermost Cretaceous interval at Deep Sea Drilling Project Site 577, *Newslett. Stratigr.*, *46*(1), 47–68, doi:10.1127/0078-0421/2013/0027.

Dickens, G. R., M. M. Castillo, and J. C. G. Walker (1997), A blast of gas in the latest Paleocene: Simulating first-order effects of massive dissociation of oceanic methane hydrate, *Geology*, *25*(3), 259–262.

Diekmann, B., and G. Kuhn (2002), Sedimentary record of the mid-Pleistocene climate transition in the southeastern South Atlantic (ODP Site 1090), *Palaeogeogr. Palaeoclimatol. Palaeoecol.*, *182*(3), 241–258.

Dunkley Jones, T., A. Ridgwell, D. J. Lunt, M. A. Maslin, D. N. Schmidt, and P. J. Valdes (2010), A Palaeogene perspective on climate sensitivity and methane hydrate instability, *Philos. Trans. R. Soc. A: Math. Phys. Eng. Sci.*, *368*(1919), 2395–2415, doi:10.1098/rsta.2010.0053.

Dutton, A., K. C. Lohmann, and M. R. Leckie (2005), Insights from the Paleogene tropical Pacific: Foraminiferal stable isotope and elemental results from Site 1209, Shatsky Rise, *Paleoceanography*, *20*, PA3004, doi:10.1029/2004PA001098.

Friedrich, O., R. D. Norris, and J. Erbacher (2012), Evolution of middle to Late Cretaceous oceans—A 55 m.y. record of Earth's temperature and carbon cycle, *Geology*, *40*(2), 107–110, doi:10.1130/G32701.1.

Galaasen, E. V., U. S. Ninnemann, N. Irvalı, H. K. F. Kleiven, Y. Rosenthal, C. Kissel, and D. A. Hodell (2014), Rapid reductions in North Atlantic deep water during the peak of the Last Interglacial Period, *Science*, *343*(6175), 1129–1132.

Galeotti, S., S. Krishnan, M. Pagani, L. Lanci, A. Gaudio, J. C. Zachos, S. Monechi, G. Morelli, and L. J. Lourens (2010), Orbital chronology of Early Eocene hyperthermals from the Contessa Road section, central Italy, *Earth Planet. Sci. Lett.*, *290*(1–2), 192–200, doi:10.1016/j.epsl.2009.12.021.

Hague, A. M., D. J. Thomas, M. Huber, R. Korty, S. C. Woodard, and L. B. Jones (2012), Convection of North Pacific deep water during the early Cenozoic, *Geology*, *40*(6), 527–530, doi:10.1130/G32886.1.

Hailwood, E. A. (1979), 11 Paleomagnetism of Late Mesozoic to Holocene sediments from the Bay of Biscay and Rockall Plateau, drilled on Ipod Leg 48, *Initial Rep. Deep Sea Drill. Proj.*, *48*(11), 305–339.

Hailwood, E. A., W. Bock, L. Costa, P. A. Depeuble, C. Müller, and D. Schnitker (1979), 58. Chronology and biostratigraphy of northeast Atlantic sediments, DSDP Leg 48, *Initial Rep. Deep Sea Drill. Proj.*, *48*(58), 1119–1141.

Hancock, H. J. L., G. R. Dickens, E. Thomas, and K. L. Blake (2007), Reappraisal of early Paleogene CCD curves: Foraminiferal assemblages and stable carbon isotopes across the carbonate facies of Perth Abyssal Plain, *Int. J. Earth Sci.*, *95*, 925–946.

Hilting, A. K., L. R. Kump, and T. J. Bralower (2008), Variations in the oceanic vertical carbon isotope gradient and their implications for the Paleocene-Eocene biological pump, *Paleoceanography*, *23*, PA3222, doi:10.1029/2007PA001458.

Huber, M., L. Sloan, and C. Shellito (2003), Early Paleogene oceans and climate: A fully coupled modeling approach using the NCAR CCSM, in *Causes and Consequences of Globally Warm Climates in the Early Paleogene*, vol. 369, edited by S. L. Wing et al., pp. 25–47, Geological Society of America, Boulder, Colo.

Hut, G. (1987), Consultants' group meeting on stable isotope reference samples for geochemical and hydrological investigations, Report to the Director General, International Atomic Energy Agency, Vienna, April 1987.

Jorissen, F. J., and I. Wittling (1999), Ecological evidence from live-dead comparisons of benthic foraminiferal faunas off Cape Blanc (Northwest Africa), *Palaeogeogr. Palaeoclimatol. Palaeoecol.*, *149*, 151–170.

Kaiho, K., K. Takeda, M. R. Petrizzo, and J. C. Zachos (2006), Anomalous shifts in tropical Pacific planktonic and benthic foraminiferal test size during the Paleocene-Eocene thermal maximum, *Palaeogeogr. Palaeoclimatol. Palaeoecol.*, *237*, 156–464.

Katz, M. E., D. R. Katz, K. G. Miller, D. K. Pak, N. J. Shackleton, and E. Thomas (2003), Early Cenozoic benthic foraminiferal isotopes: Species reliability and interspecies correction factors, *Paleoceanography*, *18*(2), 1024, doi:10.1029/2002PA000798.

Katz, M. E., B. S. Cramer, J. R. Toggweiler, G. Esmay, C. Liu, K. G. Miller, Y. Rosenthal, B. S. Wade, and J. D. Wright (2011), Impact of Antarctic Circumpolar Current development on late Paleogene ocean structure, *Science*, *332*(6033), 1076–1079, doi:10.1126/science.1202122.

Kelly, D. C., T. M. J. Nielsen, H. K. McCarren, J. C. Zachos, and U. Röhl (2010), Spatiotemporal patterns of carbonate sedimentation in the South Atlantic: Implications for carbon cycling during the Paleocene–Eocene thermal maximum, *Palaeogeogr. Palaeoclimatol. Palaeoecol.*, *293*(1–2), 30–40, doi:10.1016/j.palaeo.2010.04.027.

Kelly, D. C., T. M. J. Nielsen, and S. A. Schellenberg (2012), Carbonate saturation dynamics during the Paleocene–Eocene thermal maximum: Bathyal constraints from ODP sites 689 and 690 in the Weddell Sea (South Atlantic), *Mar. Geol.*, *303–306*, 75–86, doi:10.1016/j.margeo.2012.02.003.

Kennett, J. P., and L. D. Stott (1990), Proteus and Proto-Oceanus: Ancestral Paleogene Oceans as revealed from Antarctic stable isotopic results: ODP Leg 113, in *Proceedings of the Ocean Drilling Program, Scientific Results*, vol. 113, edited by P. Barker and J. Kennett, pp. 865–880, Ocean Drilling Program, College Station, Tex.

Knox, R. W. O'B. (1985), 34 Stratigraphic significance of volcanic ash in Paleocene and Eocene sediments at sites 549 and 550, *Initial Rep. Deep Sea Drill. Proj.*, *80*(34), 845–850.

Komar, N., R. E. Zeebe, and G. R. Dickens (2013), Understanding long-term carbon cycle trends: The late Paleocene through the early Eocene, *Paleoceanography*, *28*, 650–662, doi:10.1002/palo.20060.

Kominz, M. A., J. V. Browning, K. G. Miller, P. J. Sugarman, S. Mizintseva, and C. R. Scotese (2008), Late Cretaceous to Miocene sea-level estimates from the New Jersey and Delaware coastal plain coreholes: An error analysis, *Basin Res.*, *20*(2), 211–226, doi:10.1111/j.1365-2117.2008.00354.x.

Kroopnick, P. M. (1985), The distribution of $\delta^{13}C$ of ΣCO_2 in the world oceans, *Deep-Sea Res.*, *32*(1), 57–84.

Ledbetter, M. T. (1986), Bottom-current pathways in the Argentine Basin revealed by mean silt particle size, *Nature*, *321*, 423–425.

Ledbetter, M. T., and D. A. Johnson (1976), Increased transport of Antarctic bottom water in the Vema Channel during last ice age, *Science*, *194*, 837–839.

Leon-Rodriguez, L., and G. R. Dickens (2010), Constraints on ocean acidification associated with rapid and massive carbon injections: The early Paleogene record at ocean drilling program site 1215, equatorial Pacific Ocean, *Palaeogeogr. Palaeoclimatol. Palaeoecol.*, *298*(3–4), 409–420, doi:10.1016/j.palaeo.2010.10.029.

Loptson, C. A., D. J. Lunt, and J. E. Francis (2014), Investigating vegetation-climate feedbacks during the early Eocene, *Clim Past*, *10*, 419–436, doi:10.5194/cp-10-419-2014.

Lourens, L. J., A. Sluijs, D. Kroon, J. C. Zachos, E. Thomas, U. Röhl, J. Bowles, and I. Raffi (2005), Astronomical pacing of late Palaeocene to early Eocene global warming events, *Nature*, *435*, 1083–1087.

Lunt, D. J., P. J. Valdes, T. D. Jones, A. Ridgwell, A. Haywood, D. N. Schmidt, R. Marsh, and M. Maslin (2010), CO2-driven ocean circulation changes as an amplifier of Paleocene-Eocene thermal maximum hydrate destabilization, *Geology*, *38*(10), 875–878, doi:10.1130/G31184.1.

Lunt, D. J., A. Ridgwell, A. Sluijs, J. C. Zachos, S. Hunter, and A. Haywood (2011), A model for orbital pacing of methane hydrate destabilization during the Palaeogene, *Nat. Geosci.*, *4*(10), 775–778, doi:10.1038/ngeo1266.

Lunt, D. J., et al. (2012), A model-data comparison for a multi-model ensemble of early Eocene atmosphere-ocean simulations: EoMIP, *Clim Past*, *8*(5), 1717–1736, doi:10.5194/cp-8-1717-2012.

Lyle, M., K. A. Dadey, and J. W. Farrell (1995), The Late Miocene (11–8 Ma) eastern Pacific carbonate crash: Evidence for reorganization of deep-water circulation by the closure of the Panama Gateway, in *Proceedings of the Ocean Drilling Program, Scientific Results*, vol. 138, edited by N. G. Pisias et al., pp. 821–838, Ocean Drilling Program, College Station, Tex.

Masson, D. G., L. Montadert, and R. A. Scrutton (1985), 54. Regional geology of the Goban Spur continental margin, *Initial Rep. Deep Sea Drill. Proj.*, *80*(54), 1115–1139.

McCarren, H. K., E. Thomas, T. Hasegawa, U. Röhl, and J. C. Zachos (2008), Depth dependency of the Paleocene-Eocene carbon isotope excursion: Paired benthic and terrestrial biomarker records (Ocean Drilling Program Leg 208, Walvis Ridge), *Geochem. Geophys. Geosyst.*, *9*, Q10008, doi:10.1029/2008GC002116.

McCave, I. N., and I. R. Hall (2006), Size sorting in marine muds: Processes, pitfalls, and prospects for paleoflow-speed proxies, *Geochem. Geophys. Geosyst.*, *7*, Q10N05, doi:10.1029/2006GC001284.

McCave, I. N., B. Manighetti, and S. G. Robinson (1995), Sortable silt and fine sediment size/composition slicing: Parameters for paleocurrent speed and palaeoceanography, *Paleoceanography*, *10*(3), 593–610, doi:10.1029/94PA03039.

McCave, I. N., I. R. Hall, A. N. Antia, L. Chou, F. Dehairs, R. S. Lampitt, L. Thomsen, T. C. E. van Weering, and R. Wollast (2001), Distribution, composition and flux of particulate material over the European margin at 471–501N, *Deep Sea Res., Part II*, *48*, 3107–3139.

McInerney, F. A., and S. L. Wing (2011), The Paleocene-Eocene Thermal Maximum: A perturbation of carbon cycle, climate, and biosphere with implications for the future, *Annu. Rev. Earth Planet. Sci.*, *39*(1), 489–516, doi:10.1146/annurev-earth-040610-133431.

Miller, K. G., M. A. Kominz, J. V. Browning, J. D. Wright, G. S. Mountain, M. E. Katz, P. J. Sugarman, B. S. Cramer, N. Christie-Blick, and S. F. Pekar (2005), The Phanerozoic record of global sea-level change, *Science*, *310*(5752), 1293–1298.

Miller, K., G. Mountain, J. Wright, and J. Browning (2011), A 180-million-year record of sea level and ice volume variations from continental margin and deep-sea isotopic records, *Oceanography*, *24*(2), 40–53, doi:10.5670/oceanog.2011.26.

Montadert, L., and C. W. Poag (1985), Appendix I. Physical properties and correlation of seismic profiles with drilling results, *Initial Rep. Deep Sea Drill. Proj.*, *80*, 1219–1248.

Müller, G., and M. Gastner (1971), The "Karbonat Bombe", a simple device for the determination of the carbonate content in sediments, soils and other materials, *Neues Jahrbuch für Mineralogie Monatshefte*, *10*, 466–469.

Murphy, B., K. A. Farley, and J. C. Zachos (2010), An extraterrestrial 3He-based timescale for the Paleocene-Eocene thermal maximum (PETM) from Walvis Ridge, IODP Site 1266, *Geochim. Cosmochim. Acta*, *74*(17), 5098–5108, doi:10.1016/j.gca.2010.03.039.

Nicolo, M. J., G. R. Dickens, C. J. Hollis, and J. C. Zachos (2007), Multiple early Eocene hyperthermals: Their sedimentary expression on the New Zealand continental margin and in the deep sea, *Geology*, *35*(8), 699–702.

Nunes, F., and R. D. Norris (2006), Abrupt reversal in ocean overturning during the Palaeocene/Eocene warm period, *Nature*, *439*, 60–63, doi:10.1038/nature04386.

Pak, D. K., and K. G. Miller (1992), Paleocene to Eocene benthic foraminiferal isotopes and assemblages: Implications for deepwater circulation, *Paleoceanography*, *7*(4), 405–422, doi:10.1029/92PA01234.

Pälike, H., et al. (2012), A Cenozoic record of the equatorial Pacific carbonate compensation depth, *Nature*, *488*(7413), 609–614, doi:10.1038/nature11360.

Pardo, A., G. Keller, and H. Oberhänsli (1999), Paleoecologic and paleoceanographic evolution of the Tethyan realm during the Paleocene-Eocene transition, *J. Foraminiferal Res.*, *29*(1), 37–57.

Raffi, I., J. Backman, and H. Pälike (2005), Changes in calcareous nannofossil assemblages across the Paleocene/Eocene transition from the paleo-equatorial Pacific Ocean, *Palaeogeogr. Palaeoclimatol. Palaeoecol.*, *226*(1–2), 93–126, doi:10.1016/j.palaeo.2005.05.006.

Rathmann, S., and H. Kuhnert (2008), Carbonate ion effect on Mg/Ca Sr/Ca and stable isotopes on the benthic foraminifera Oridorsalis umbonatus off Namibia, *Mar. Micropaleontol.*, *66*, 120–133, doi:10.1016/j.marmicro.2007.08.001.

Rea, D. K. (1994), The paleoclimatic record provided by eolian deposition in the deep sea: The geological history of wind, *Rev Geophys.*, *32*(2), 159–195, doi:10.1029/93RG03257.

Ridgwell, A., and R. E. Zeebe (2005), The role of the global carbonate cycle in the regulation and evolution of the Earth system, *Earth Planet. Sci. Lett.*, *234*(3–4), 299–315, doi:10.1016/j.epsl.2005.03.006.

Roberts, C. D., A. N. Legrande, and A. K. Tripati (2009), Climate sensitivity to Arctic seaway restriction during the early Paleogene, *Earth Planet. Sci. Lett.*, *286*(3–4), 576–585, doi:10.1016/j.epsl.2009.07.026.

Roberts, C. D., A. N. Legrande, and A. K. Tripati (2011), Sensitivity of seawater oxygen isotopes to climatic and tectonic boundary conditions in an early Paleogene simulation with GISS ModelE-R, *Paleoceanography*, *26*, PA4203, doi:10.1029/2010PA002025.

Robinson, S. A., and D. Vance (2012), Widespread and synchronous change in deep-ocean circulation in the North and South Atlantic during the Late Cretaceous, *Paleoceanography*, *27*, PA1102, doi:10.1029/2011PA002240.

Röhl, U., T. J. Bralower, R. D. Norris, and G. Wefer (2000), New chronology for the late Paleocene thermal maximum and its environmental implications, *Geology*, *28*(10), 927–930.

Röhl, U., R. D. Norris, and J. G. Ogg (2003), Cyclostratigraphy of upper Paleocene and lower Eocene sediments at Blake Nose Site 1051 (western North Atlantic), *Geol. Soc. Am. Spec. Pap.*, *369*, 567–588.

Schmiedl, G., and A. Mackensen (2006), Multispecies stable isotopes of benthic foraminifers reveal past changes of organic matter decomposition and deepwater oxygenation in the Arabian Sea, *Paleoceanography*, *21*, PA4213, doi:10.1029/2006PA001284.

Sexton, P. F., P. A. Wilson, and R. D. Norris (2006), Testing the Cenozoic multisite composite δ18O and δ13C curves: New monospecific Eocene records from a single locality, Demerara Rise (Ocean Drilling Program Leg 207), *Paleoceanography*, *21*, PA2019, doi:10.1029/2005PA001253.

Sexton, P. F., R. D. Norris, P. A. Wilson, H. Pälike, T. Westerhold, U. Röhl, C. T. Bolton, and S. J. Gibbs (2011), Eocene global warming events driven by ventilation of oceanic dissolved organic carbon, *Nature*, *471*(7338), 349–352, doi:10.1038/nature09826.

Shackleton, N. J., and M. A. Hall (1997), The Late Miocene stable isotope record, Site 926, in *Proceedings of the Ocean Drilling Program, Scientific Results*, vol. 154, edited by N. J. Shackleton et al., pp. 367–373, Ocean Drilling Program, College Station, Tex.

Shackleton, N. J., M. A. Hall, and A. Boersma (1984), 15. Oxygen and carbon isotope data from Leg 74 foraminifers, *Initial Rep. Deep Sea Drill. Proj.*, *74*(15), 599–612.

Sluijs, A., et al. (2008), Eustatic variations during the Paleocene-Eocene greenhouse world, *Paleoceanography*, *23*, PA4216, doi:10.1029/2008PA001615.

Sluijs, A., et al. (2009), Warm and wet conditions in the Arctic region during Eocene Thermal Maximum 2, *Nat. Geosci.*, *2*(11), 1–4, doi:10.1038/ngeo668.
Sluijs, A., R. E. Zeebe, P. K. Bijl, and S. M. Bohaty (2013), A middle Eocene carbon cycle conundrum, *Nat. Geosci.*, *6*(6), 429–434, doi:10.1038/ngeo1807.
Speijer, R. P., C. Scheibner, P. Stassen, and A. M. M. Morsi (2012), Response of marine ecosystems to deep-time global warming: A synthesis of biotic patterns across the Paleocene-Eocene thermal maximum (PETM), *Austrian J. Earth Sci.*, *105*(1), 6–16.
Stap, L., A. Sluijs, E. Thomas, and L. J. Lourens (2009), Patterns and magnitude of deep sea carbonate dissolution during Eocene Thermal Maximum 2 and H2, Walvis Ridge, southeastern Atlantic Ocean, *Paleoceanography*, *24*, PA1211, doi:10.1029/2008PA001655.
Stap, L., L. J. Lourens, E. Thomas, A. Sluijs, S. M. Bohaty, and J. C. Zachos (2010), High-resolution deep-sea carbon and oxygen isotope records of Eocene Thermal Maximum 2 and H2, *Geology*, *38*(7), 607–610, doi:10.1130/G30777.1.
Stassen, P., E. Steurbaut, A.-M. M. Morsi, P. Schulte, and R. P. Speijer (2012), Biotic impact of Eocene thermal maximum 2 in a shelf setting (Dababiya, Egypt), *Austrian J. Earth Sci.*, *105*(1), 154–160.
Stocker, T. F., and D. G. Wright (1991), Rapid transitions of the ocean's deep circulation induced by changes in surface water fluxes, *Nature*, *351*(6329), 729–732.
Stuecker, M. F., and R. E. Zeebe (2010), Ocean chemistry and atmospheric CO_2 sensitivity to carbon perturbations throughout the Cenozoic, *Geophys. Res. Lett.*, *37*, L03609, doi:10.1029/2009GL041436.
Takeda, K., and K. Kaiho (2007), Faunal turnovers in central Pacific benthic foraminifera during the Paleocene–Eocene thermal maximum, *Palaeogeogr. Palaeoclimatol. Palaeoecol.*, *251*(2), 175–197.
Thomas, E. (1990), Late Cretaceous through Neogene deep-sea benthic foraminifers (Maud Rise, Weddell Sea, Antarctica), in *Proceedings of the Ocean Drilling Program, Scientific Results*, vol. 113, edited by P. F. Barker, pp. 571–594, Ocean Drilling Program, College Station, Tex.
Thomas, E. (2007), Cenozoic mass extinctions in the deep sea: What perturbs the largest habitat on Earth?, *Geol. Soc. Am. Spec. Pap.*, *424*, 1–23.
Thomas, D. J., and T. J. Bralower (2005), Sedimentary trace element constraints on the role of North Atlantic Igneous Province volcanism in late Paleocene-early Eocene environmental change, *Mar. Geol.*, *217*, 233–254, doi:10.1016/j.margeo.2005.02.009.
Thomas, E., and N. J. Shackleton (1996), The Paleocene-Eocene benthic foraminiferal extinction and stable isotope anomalies, *Geol. Soc. London Spec. Publ.*, *101*, 101–441.
Thomas, D. J., T. J. Bralower, and C. E. Jones (2003), Neodymium isotopic reconstruction of late Paleocene-early Eocene thermohaline circulation, *Earth Planet. Sci. Lett.*, *209*(3–4), 309–322, doi:10.1016/S0012-821X(03)00096-7.
Thomas, D. J., M. Lyle, T. C. Moore, and D. K. Rea (2008), Paleogene deepwater mass composition of the tropical Pacific and implications for thermohaline circulation in a greenhouse world, *Geochem. Geophys. Geosyst.*, *9*, Q02002, doi:10.1029/2007GC001748.
Tripati, A. K., and H. Elderfield (2005), Deep-sea temperature and circulation changes at the Paleocene-Eocene thermal maximum, *Science*, *308*, 1894–1898.
Uchikawa, J., and R. E. Zeebe (2010), Examining possible effects of seawater pH decline on foraminiferal stable isotopes during the Paleocene-Eocene Thermal Maximum, *Paleoceanography*, *25*, PA2216, doi:10.1029/2009PA001864.
Via, R. K., and D. J. Thomas (2006), Evolution of Atlantic thermohaline circulation: Early Oligocene onset of deep-water production in the North Atlantic, *Geology*, *34*(6), 441, doi:10.1130/G22545.1.
van Andel, T. H., G. R. Heath, and T. C. Moore (1975), Cenozoic history and paleoceanography of the central equatorial Pacific Ocean, *GSA Mem.*, *143*, 134.
van Weering, T. C. E., I. R. Hall, H. C. de Stigter, I. N. McCave, and L. Thomsen (1998), Recent sediments, sediment accumulation and carbon burial at Goban Spur, NW European Continental Margin (47 -50°N), *Prog. Oceanogr.*, *42*, 5–35.
Westerhold, T., U. Röhl, J. Laskar, I. Raffi, J. Bowles, L. J. Lourens, and J. C. Zachos (2007), On the duration of magnetochrons C24r and C25n and the timing of early Eocene global warming events: Implications from the Ocean Drilling Program Leg 208 Walvis Ridge depth transect, *Paleoceanography*, *22*, PA2201, doi:10.1029/2006PA001322.
Westerhold, T., U. Röhl, H. K. McCarren, and J. C. Zachos (2009), Latest on the absolute age of the Paleocene–Eocene Thermal Maximum (PETM): New insights from exact stratigraphic position of key ash layers +19 and −17, *Earth Planet. Sci. Lett.*, *287*(3–4), 412–419, doi:10.1016/j.epsl.2009.08.027.
Westerhold, T., U. Röhl, and J. Laskar (2012), Time scale controversy: Accurate orbital calibration of the early Paleogene, *Geochem. Geophys. Geosyst.*, *13*, Q06015, doi:10.1029/2012GC004096.
Winguth, A., C. Shellito, C. Shields, and C. Winguth (2010), Climate response at the Paleocene–Eocene Thermal Maximum to Greenhouse Gas Forcing—A model study with CCSM3, *J. Clim.*, *23*(10), 2562–2584, doi:10.1175/2009JCLI3113.1.
Winguth, A. M. E., E. Thomas, and C. Winguth (2012), Global decline in ocean ventilation, oxygenation, and productivity during the Paleocene-Eocene Thermal Maximum: Implications for the benthic extinction, *Geology*, *40*(3), 263–266, doi:10.1130/G32529.1.
Zachos, J. C., L. D. Stott, and K. C. Lohmann (1994), Evolution of early Cenozoic marine temperatures, *Paleoceanography*, *9*(2), 353–387, doi:10.1029/93PA03266.
Zachos, J. C., D. Kroon, P. Blum, and S. S. Party (2004), 3. Site 1262, in *Proceedings of the Ocean Drilling Program, Initial Reports*, vol. 208, pp. 1–92, Ocean Drilling Program, College Station, Tex.
Zachos, J. C., U. Röhl, S. A. Schellenberg, and A. Sluijs (2005), Rapid acidification of the ocean during the Paleocene-Eocene Thermal Maximum, *Science*, *308*, 1611–1615.
Zachos, J. C., G. R. Dickens, and R. E. Zeebe (2008), An early Cenozoic perspective on greenhouse warming and carbon-cycle dynamics, *Nature*, *451*(7176), 279–283.
Zachos, J. C., H. K. McCarren, B. Murphy, U. Röhl, and T. Westerhold (2010), Tempo and scale of late Paleocene and early Eocene carbon isotope cycles: Implications for the origin of hyperthermals, *Earth Planet. Sci. Lett.*, *299*, 242–249.
Zarriess, M., and A. Mackensen (2011), Testing the impact of seasonal deposition of phytodetritus strongly affects $\delta^{13}C$ of epibenthic foraminifer Cibicidoides wuellerstorfi: A 31,000-year high-resolution record from the Northwest African continental slope, 1–21.
Zeebe, R. E. (2012), History of seawater carbonate chemistry, atmospheric CO2, and ocean acidification, *Annu. Rev. Earth Planet. Sci.*, *40*(1), 141–165, doi:10.1146/annurev-earth-042711-105521.
Zeebe, R. E. (2013), What caused the long duration of the Paleocene-Eocene Thermal Maximum?, *Paleoceanography*, *28*, 440–452, doi:10.1002/palo.20039.
Zeebe, R. E., and J. C. Zachos (2007), Reversed deep-sea carbonate ion basin gradient during Paleocene-Eocene thermal maximum, *Paleoceanography*, *22*, PA3201, doi:10.1029/2006PA001395.
Zeebe, R. E., J. C. Zachos, and G. R. Dickens (2009), Carbon dioxide forcing alone insufficient to explain Palaeocene–Eocene Thermal Maximum warming, *Nat. Geosci.*, *2*(8), 576–580, doi:10.1038/ngeo578.
Ziegler, M., P. Diz, I. R. Hall, and R. Zahn (2013), Millennial-scale changes in atmospheric CO2 levels linked to the Southern Ocean carbon isotope gradient and dust flux, *Nat. Geosci.*, *3*(4), 1–5, doi:10.1038/ngeo1782.